Since January 2020 Elsevier has created a COVID-19 resource centre with free information in English and Mandarin on the novel coronavirus COVID-19. The COVID-19 resource centre is hosted on Elsevier Connect, the company's public news and information website.

Cell Reports

Article

In vivo characterization of emerging SARS-CoV-2 variant infectivity and human antibody escape potential

Graphical abstract

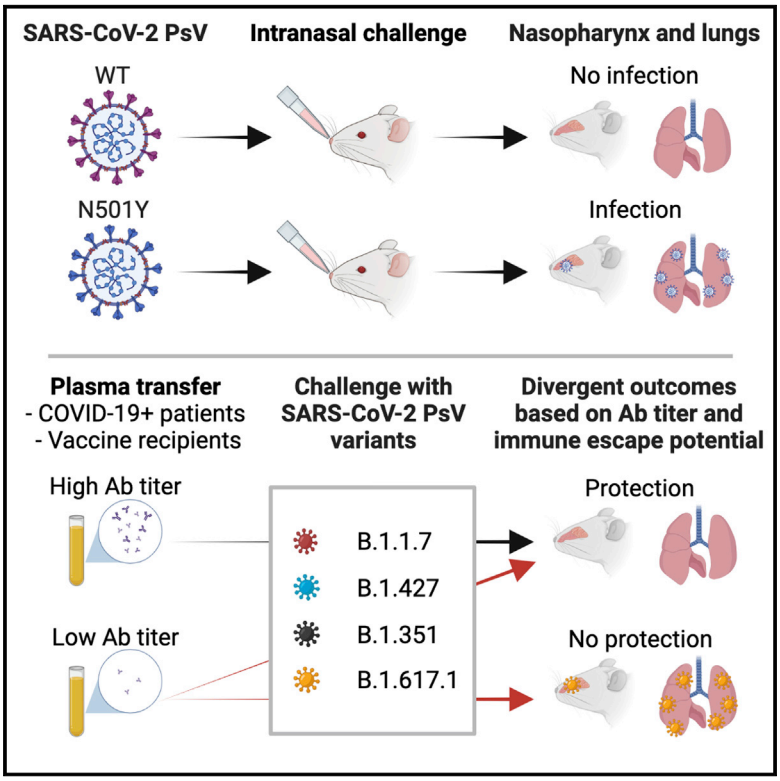

Highlights

- N501Y RBD SARS-CoV-2 PsVs achieve high-level infection in murine respiratory tract
- South Africa and India variant PsVs attain the most robust airway infection in mice
- SARS-CoV-2 variants carrying E484 perturbations exhibit immune escape *in vivo*
- High-titer COVID-19+ or vaccinated individuals control emerging variants the strongest

Authors

Brandon Lam, Yu Jui Kung, John Lin, ..., Richard B.S. Roden, Tzyy-Choou Wu, Chien-Fu Hung

Correspondence

chung2@jhmi.edu

In brief

Lam et al. develop a model of SARS-CoV-2 infection in laboratory mice. This allows researchers to study the threat of emerging variants in a more physiological context than by using cell culture systems. Interactions between SARS-CoV-2 variants and immunity are explored in the airway of mice.

Lam et al., 2021, Cell Reports *37*, 109838
October 19, 2021
https://doi.org/10.1016/j.celrep.2021.109838

CellPress

Cell Reports

CellPress
OPEN ACCESS

Article

In vivo characterization of emerging SARS-CoV-2 variant infectivity and human antibody escape potential

Brandon Lam,[1,2] Yu Jui Kung,[1] John Lin,[1] Ssu-Hsueh Tseng,[1] Ya Chea Tsai,[1] Liangmei He,[1] Gianni Castiglione,[3] Emily Egbert,[4] Elia J. Duh,[3] Evan M. Bloch,[1] Aaron A.R. Tobian,[1] Aaron M. Milstone,[4,5,6] Richard B.S. Roden,[1,7,8] Tzyy-Choou Wu,[1,7,8,9] and Chien-Fu Hung[1,7,10,*]

[1]Department of Pathology, Johns Hopkins University School of Medicine, Baltimore, MD 21205, USA
[2]Graduate Program in Immunology, Johns Hopkins University School of Medicine, Baltimore, MD 21205, USA
[3]Department of Ophthalmology, Johns Hopkins University School of Medicine, Baltimore, MD 21205, USA
[4]Division of Infectious Diseases, Department of Pediatrics, Johns Hopkins University School of Medicine, Baltimore, MD 21205, USA
[5]Department of Epidemiology, Johns Hopkins Bloomberg School of Public Health, Baltimore, MD 21205, USA
[6]Department of Hospital Epidemiology and Infection Control, The Johns Hopkins Hospital, Baltimore, MD 21205, USA
[7]Department of Oncology, Johns Hopkins University School of Medicine, Baltimore, MD 21205, USA
[8]Department of Obstetrics and Gynecology, Johns Hopkins University School of Medicine, Baltimore, MD 21205, USA
[9]Molecular Microbiology and Immunology, Johns Hopkins University School of Medicine, Baltimore, MD 21205, USA
[10]Lead contact
*Correspondence: chung2@jhmi.edu
https://doi.org/10.1016/j.celrep.2021.109838

SUMMARY

As severe acute respiratory syndrome coronavirus 2 (SARS-CoV-2) spreads, variants with enhanced virulence and transmissibility have emerged. Although *in vitro* systems allow rapid characterization, they do not fully recapitulate the dynamic interaction of virions and neutralizing antibodies in the airway. Here, we demonstrate that the N501Y variant permits respiratory infection in unmodified mice. We utilize N501Y to survey *in vivo* pseudovirus infection dynamics and susceptibility to reinfection with the L452R (Los Angeles), K417N + E484K (South Africa), and L452R + K417N + E484Q (India) variants. Human coronavirus disease 2019 (COVID-19)+ or vaccinated antibody isotypes, titers, variant receptor binding domain (RBD) binding, and neutralization potential are studied, revealing numerous significant correlations. Immune escape of the K417N + E484K variant is observed because infection can be appreciated in the nasopharynx, but not lungs, of mice transferred with low-antibody-tier plasma. Conversely, near-complete protection is observed in animals receiving high-antibody-tier plasma, a phenomenon that can only be appreciated *in vivo*.

INTRODUCTION

Coronavirus disease 2019 (COVID-19), the disease caused by severe acute respiratory syndrome coronavirus 2 (SARS-CoV-2), has infected more than 167 million people and killed more than 3.4 million people in 223 countries as of late May 2021 (WHO, 2021a), underscoring the urgency of COVID-19 research. The SARS-CoV-2 spike protein complex comprises two mature independently functioning proteins: S1 containing the receptor binding domain (RBD) and the S2 stalk (Shang et al., 2020a). Interaction of spike with host angiotensin-converting enzyme 2 (ACE2) mediates viral attachment and subsequent infection (Shang et al., 2020b). Given the crucial role of spike, specifically the RBD, in infectivity and antibody-mediated neutralization of SARS-CoV-2, it has been explored extensively as the major COVID-19 preventative vaccine target (Forni et al., 2021; WHO, 2021a), leading to emergency use authorization of three vaccines in the United States (CDC, 2021a).

Although the Wuhan variant of SARS-CoV-2 spread rapidly, more contagious variants have emerged and pose even greater public health risks. For example, the D614G mutation displayed heightened infectivity and quickly became the most prevalent form spreading early in the COVID-19 pandemic (Korber et al., 2020; Plante et al., 2021; Yurkovetskiy et al., 2020). Recently, SARS-CoV-2 variants that carry the N501Y mutation have been spreading in the United Kingdom (WHO, 2021c), Brazil (Sabino et al., 2021), South Africa (CDC, 2021b), and India (CDC, 2021b) and appear to have heightened transmissibility in humans (Li et al., 2020; WHO, 2021b). In the United States, a variant has also been identified in Los Angeles (Zhang et al., 2021), along with numerous others being identified and characterized currently.

As these variants continue to emerge, it is crucial for virologists to be able to evaluate any changes in SARS-CoV-2 virulence and transmissibility mediated by these mutations. In addition, the immune escape potential of any emerging perturbations must be evaluated in individuals who received a COVID-19 vaccine or

Table 1. Summary of SARS-CoV-2 PsVs used to model emerging variants

SARS-CoV-2 PsV variant	Pango lineage	WHO designation	First noted outbreak
N501Y + D614G	B.1.1.7	alpha	United Kingdom
N501Y + L452R + D614G	B.1.427	no designation	Los Angeles, CA, United States
N501Y + K417N + E484K + D614G	B.1.351	beta	South Africa
N501Y + L452R + K417N + E484Q + D614G	B.1.617.1	kappa	India

were infected previously with SARS-CoV-2. This information is critical for delineating COVID-19-related public health guidance moving forward. Typically, *in vitro* neutralization assays are used to evaluate these critical factors using SARS-CoV-2 virus or SARS-CoV-2 pseudovirions (Harrison et al., 2020; Jia et al., 2021; Shang et al., 2020b; Zost et al., 2020).

An area of growing research interest is animal modeling of COVID-19 to better understand physiological and anatomical aspects of infection and immune escape. Although some mammals can be inoculated successfully with SARS-CoV-2, laboratory mice are the most desirable research tool because of their low cost, facility support, and ease of use (Muñoz-Fontela et al., 2020). However, mice cannot be infected natively with SARS-CoV-2 because of RBD-mouse ACE2 (mACE2) incompatibility. To overcome this, investigators have utilized numerous strategies to introduce human ACE2 (hACE2) to mice, including transgenic mice (McCray et al., 2007) and AdV5-hACE2 transduction (Hassan et al., 2020; Singh et al., 2020; Sun et al., 2020). Alternatively, SARS-CoV-2 can be engineered to achieve infection in mice. This was achieved using *in vivo* passaging and selection of preparations that are mouse tropic because of RBD variant selection (Gu et al., 2020). In this study, we explore an *in vivo* method to study SARS-CoV-2 variant pseudovirion infectivity and immune escape potential in individuals infected previously with COVID-19 or receiving COVID-19 vaccines. A summary of SARS-CoV-2 variants utilized in the study can be found in Table 1.

RESULTS

Development of an ABSL-2 *in vivo* model of SARS-CoV-2 infection using the United Kingdom B.1.1.7 variant

Given the heightened infectivity and public health threat of the United Kingdom B.1.1.7 SARS-CoV-2 variant, we sought to examine the potential for murine tropism and characterize the utility of B.1.1.7 spike mutations, notably N501Y, in mouse modeling. This mutation was also present among 4 nonsynonymous mutations in a mouse-infective variant selected through sequential *in vivo* passaging (Gu et al., 2020). Although molecular visualization of SARS-CoV-2 RBD binding to hACE2 shows differences between the wild-type (WT) or N501Y RBD variant that could explain higher infectivity (Figure 1A; Fratev, 2020; Santos and Passos, 2021), the interaction between mACE2 and the N501Y RBD variant reveals major differences (Figure 1B). No interactions are predicted between the WT RBD and mACE2, but new non-covalent π-π interactions are predicted between H353 and Y41 of mACE2 and Y501 of the RBD (Figure S1A). To query these interactions' biological significance, we performed surface plasmon resonance and cytometric binding assays between hACE2-expressing 293 cells and the WT or N501Y RBD. The N501Y-RBD displayed heightened binding and a lower K_d with hACE2 compared with the WT RBD in both binding assays (Figure 1C; Figures S1D and S1E). Strikingly, when comparing WT or N501Y RBD binding with mACE2, the WT RBD did not bind, but the N501Y RBD bound strongly with a K_d of 47.6 nM (Figure 1D). This binding pattern was confirmed using RBD-Fc and N501Y RBD Fc protein (Figures S1B and S1C). Moreover, we compared the binding qualities of RBD-Fc and N501Y RBD-Fc with bat ACE2 (*Rhinolophus sinicus*, XM_019746337.1), dog ACE2, pangolin ACE2, mACE2, and hACE2, revealing that the mouse was the mammalian host most affected by the N501Y mutation (Figures S1F and S1G).

With this impetus, we generated Lentivirus (Lenti) and vesicular stomatitis virus (VSV) pseudoviruses (PsVs) incorporating spike variants, including WT and D614G with or without the N501Y mutation, to determine how N501Y would change the infection potential on hACE2- or mACE2-expressing cells (Figure S2A; Table S1). All PsVs had a 19-amino-acid deletion (19del), which has been shown to be critical in SARS-CoV/CoV-2 PsVs (Giroglou et al., 2004; Hu et al., 2020). The activity of non-19del WT and N501Y PsVs was also determined (Figures S2C, S2D, and S3A–S3E). When examining Lenti (Figure 1E) or VSV (Figure 1F) PsV infection on hACE2+ cells, D614G and N501Y + D614G (alpha variant) displayed high-level infectivity, with N501Y + D614G VSV PsVs displaying slightly superior infection (Figure 1F). All PsVs displayed some level of infection on hACE2+ cells. In contrast, mACE2+ cells could only be infected productively with PsVs carrying the N501Y mutation, with N501Y + D614G VSV PsV performing the best (Figure 1F). VSV PsV infectivity consistently outperformed that of Lenti PsVs, with an approximate 2-log increase in relative luminescence units (RLUs). Hence, we pursued the modeling potential of N501Y SARS-CoV-2 VSV PsVs *in vivo*.

Given the notable enhancement N501Y provides to RBD binding and PsV infection on mACE2+ cells, we investigated whether this mutation would allow a species switch to occur *in vivo*. Following treatment with anti-IFNAR1, a standard practice prior to SARS-CoV-2 murine challenge (Hassan et al., 2020; Sun et al., 2020), BALB/c mice were challenged intranasally with VSV PsVs and imaged via *in vivo* imaging system (IVIS) for luciferase activity. Strikingly, N501Y + D614G PsV challenge led to significant infection in the nasopharynx and lungs (Figures 1G–1I), whereas N501Y PsV displayed lower-level infection, presumably because of the lack of D614G-mediated infection enhancement. Infection was confirmed by fluorescence microscopy and *ex vivo* imaging (Figures S2F–S2I). No murine infection was noted in the absence of N501Y (Figures 1G–1I), supporting its indispensable role. In addition, infection was observed when applying this regimen in C57BL/6 mice (Figures S3A and S3B). These results confirm that the N501Y mutation allows SARS-CoV-2 PsVs to

CellPress
OPEN ACCESS

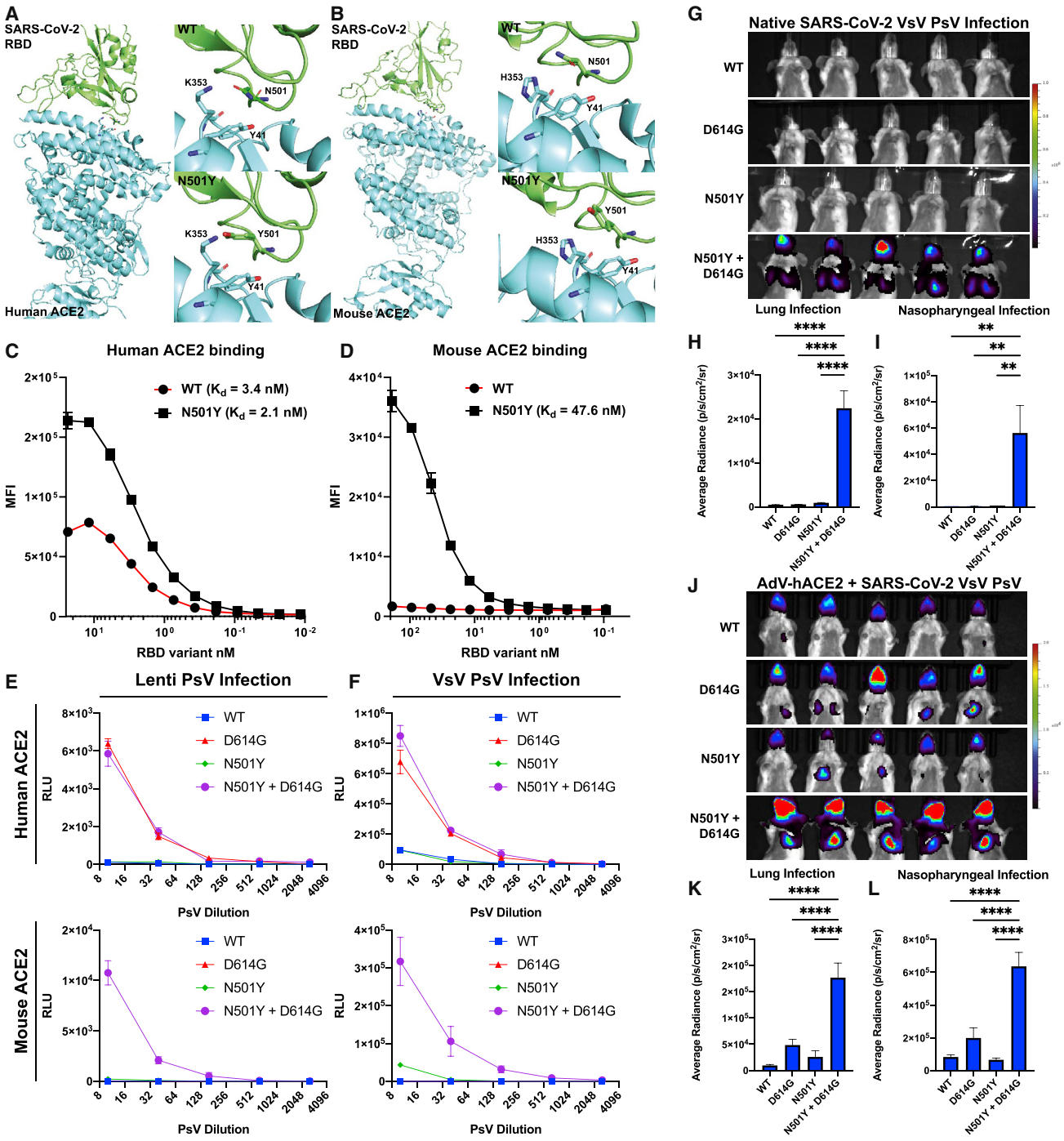

Figure 1. The SARS-CoV-2 N501Y variant VSV-based murine model

(A) Molecular visualization of the interaction between the SARS-CoV-2 RBD located in the spike protein (green) and hACE2 (blue). Critical residues involved in binding of the RBD and hACE2 that are of significance in our model, K353 and Y41 on hACE2 and N501 on the RBD, are labeled. Top: interaction between the WT RBD and hACE2. Bottom: the N501Y-RBD variant.

(B) Visualization consistent with (A), but hACE2 is replaced with mACE2. Critical residues are labeled, including H353 and Y41 of mACE2 and N501 (WT) or Y501 (variant) of the RBD.

(C and D) Binding curves of the WT or N501Y variant RBD with 293 cells expressing hACE2 (C) or mACE2 (D). Hexa-Histidine (6HIS)-tagged WT or N501Y RBD proteins were titrated on a 2-fold scale according to values on the x axis. Following binding, cells were stained with saturating concentrations of anti-HIS-phycoerythrin (PE), washed, fixed, and analyzed via flow cytometry (n = 3 per dilution point). K_d was determined using the curve fit function in GraphPad Prism 9. K_d for hACE2 binding: WT (K_d = 3.4 nM), N501Y (K_d = 2.1 nM). K_d for mACE2 binding: WT (K_d cannot be determined), N501Y (K_d = 47.6 nM).

(legend continued on next page)

species switch to the mouse and that it can permit rapid *in vivo* infection as a research tool.

We also aimed to characterize the *in vivo* infection potential of N501Y-bearing PsVs on hACE2+ tissues. Following previous methods (Hassan et al., 2020; Sun et al., 2020), AdV5-hACE2 was transduced intranasally to introduce hACE2 to airway cells 4 days prior to PsV challenge. Upon imaging, infection was seen in the nasopharynx and lungs of SARS-CoV-2 PsV-challenged mice (Figures 1J–1L; Figures S3C–S3E). Importantly, the presence of the N501Y mutation in PsVs resulted in higher luciferase activity in hACE2-transduced mice. Under mACE2 and hACE2 conditions, the role of 19del in PsV infection *in vivo* was explored, revealing that, consistent with previous studies, the presence of the 19del led to significantly higher infection *in vivo*. Accordingly, we utilized PsVs carrying the 19del in the remainder of our studies. This supports the theories that N501Y leads to higher hACE2- and mACE2-dependent infection potential *in vivo* and that SARS-CoV-2 VSV PsVs serve as an easy-to-use Animal Biosafety Level 2 (ABSL-2) system to robustly study infectivity through hACE2 or mACE2.

Following establishment of our N501Y SARS-CoV-2 VSV system, we sought to test its applicability and manipulability using convalescent plasma transfer, a classic method for infection neutralization (Katz, 2021). To query its feasibility in our system, N501Y + D614G PsV was preincubated with plasma from individuals infected previously with COVID-19, mice vaccinated with RBD-Fc, or control humans or mice. Plasma/PsV mixtures were then added to mACE2+ or hACE2+ cells. Human and mouse plasma samples were able to block mACE2- and hACE2-specific infection in a titratable manner (Figures 2A and 2B). Next, we explored this system *in vivo*. BALB/c mice received adoptive transfer of normal human, previously COVID-19+ human, or RBD-Fc mouse antisera. Mice vaccinated with RBD-Fc were also utilized. All groups were then challenged with N501Y + D614G VSV PsV. Significant blocking of infection was observed (Figures 2C–2E), with no effect noted in the control arms. These data support the hypothesis that N501Y variant SARS-CoV-2 PsVs can be used to model infection and spike antibody-mediated prophylactic immunity. Following transduction with AdV5-hACE2 *in vivo*, neutralization findings similar to those in Figures 2C–2E were observed (Figures 2F–2H).

In vivo infectivity of PsVs incorporating crucial mutations of the Los Angeles and South Africa SARS-CoV-2 variants

Having established that our system is capable of modeling infection of SARS-CoV-2 and antibody-mediated neutralization *in vivo*, we sought to apply our system to query the infectivity of emerging spike mutations that pose serious public health threats. We generated VSV PsVs carrying L452R (Los Angeles variant) or K417N + E484K (South Africa, beta variant) alongside N501Y + D614G (Figure S2B). *In vitro* infection assays reveal that PsVs carrying Los Angeles N501Y + L452R + D614G and South Africa N501Y + K417N + E484K + D614G spike mutations are infective through hACE2 (Figure 3A) and mACE2 (Figure 3B). PsVs with the K417N + E484K mutations appeared to have heightened infection, as determined by RLUs. To examine the relevance of this finding *in vivo*, BALB/c mice were infected according to our previous method. Strikingly, South Africa N501Y + K417N + E484K + D614G PsVs demonstrated significantly higher infection in the nasopharynx and lungs (Figures 3C–3E) compared with Los Angeles N501Y + L452R + D614G and N501Y + D614G PsVs. Similar infection was observed in C57BL/6 mice (Figures S3F–S3H).

Murine susceptibility to PsV rechallenge with emerging SARS-CoV-2 variants

In addition to modeling infectivity, we sought to determine whether our system could be used to model SARS-CoV-2 reinfection, a phenomenon observed in some individuals (Hansen et al., 2021). With the rise of SARS-CoV-2 mutants, the potential for immune escape from antibodies engendered during a primary response increases, and susceptibility to a secondary infection becomes more likely. This is especially true when the mutations arise in crucial antibody binding domains in the RBD. To explore this, we infected mice with N501Y + D614G PsVs. Two weeks later, mice were rechallenged with N501Y + D614G or N501Y + K417N + E484K + D614G PsV, given that the E484K mutation has been linked to antibody-mediated immune escape and virulence of the South Africa variant. A baseline RLU for primary infection with N501Y + D614G or N501Y + K417N + E484K + D614G PsV was set as the average RLU of 10 mice infected with the respective PsV. Setting the baseline

(E) Pseudotyped SARS-CoV-2 lentivirus *in vitro* infection assay. Luciferase-expressing SARS-CoV-2 variant Lenti PsVs, including (1) WT, (2) D614G, (3) N501Y, and (4) N501Y + D614G (all having a 19-amino-acid [aa] deletion) were normalized to the total amount of S protein via western blot, titrated across a 2-fold range as indicated on the x axis, and then added to hACE+, mACE2+, or non-transfected 293 cells that were seeded 24 h prior to infection. 48 h later, cells were lysed and analyzed for luciferase activity via GloMax as a readout of infection level (n = 3).

(F) Pseudotyped SARS-CoV-2 VSV *in vitro* infection assay following the same methodology as in (E) (n = 3).

(G) Infection of SARS-CoV-2 VSV-based PsVs in BALB/c mice. 24 h prior to challenge, mice were administered 500 μg of anti-interferon alpha and beta receptor subunit 1 (anti-IFNAR1). Then mice were anesthetized with 2.5% vaporized isoflurane and administered normalized amounts of the indicated PsVs intranasally, including (1) WT, (2) D614G, (3) N501Y, and (4) N501Y + D614G . 24 h later, mice were administered 80 μg of D-luciferin intranasally and 100 μg intravenously and then imaged via IVIS for 5 min with an open emission filter. All groups were set to the same scale during image processing (n = 5).

(H and I) Quantification of signal in the lungs (H) and nasopharyngeal passage (I) of mice infected with the indicated PsVs.

(J) Infection of SARS-CoV-2 VSV-based PsVs in BALB/c mice following AdV5-hACE2 transduction. Mice were treated identically as in (G)–(I), except 4 days before VSV PsV challenge, mice were administered equal amounts of AdV5-hACE2 intranasally following anesthetization with 2.5% vaporized isoflurane. SARS-CoV-2 VSV PsV infection groups include (1) WT, (2) D614G, (3) N501Y, and (4) N501Y + D614G.

(K and L) Quantification of signal in the lungs (K) and nasopharyngeal passage (L) of mice transduced with AdV5-hACE2 and challenged with the indicated SARS-CoV-2 VSV PsVs (n = 5).

Experiments were performed in 3 technical replicates (C–F) or 5 biological replicates (G–L). Mean ± SEM is shown. *, **, and *** indicate p values less than 0.05, 0.01, and 0.001, respectively; N.S., not significant.

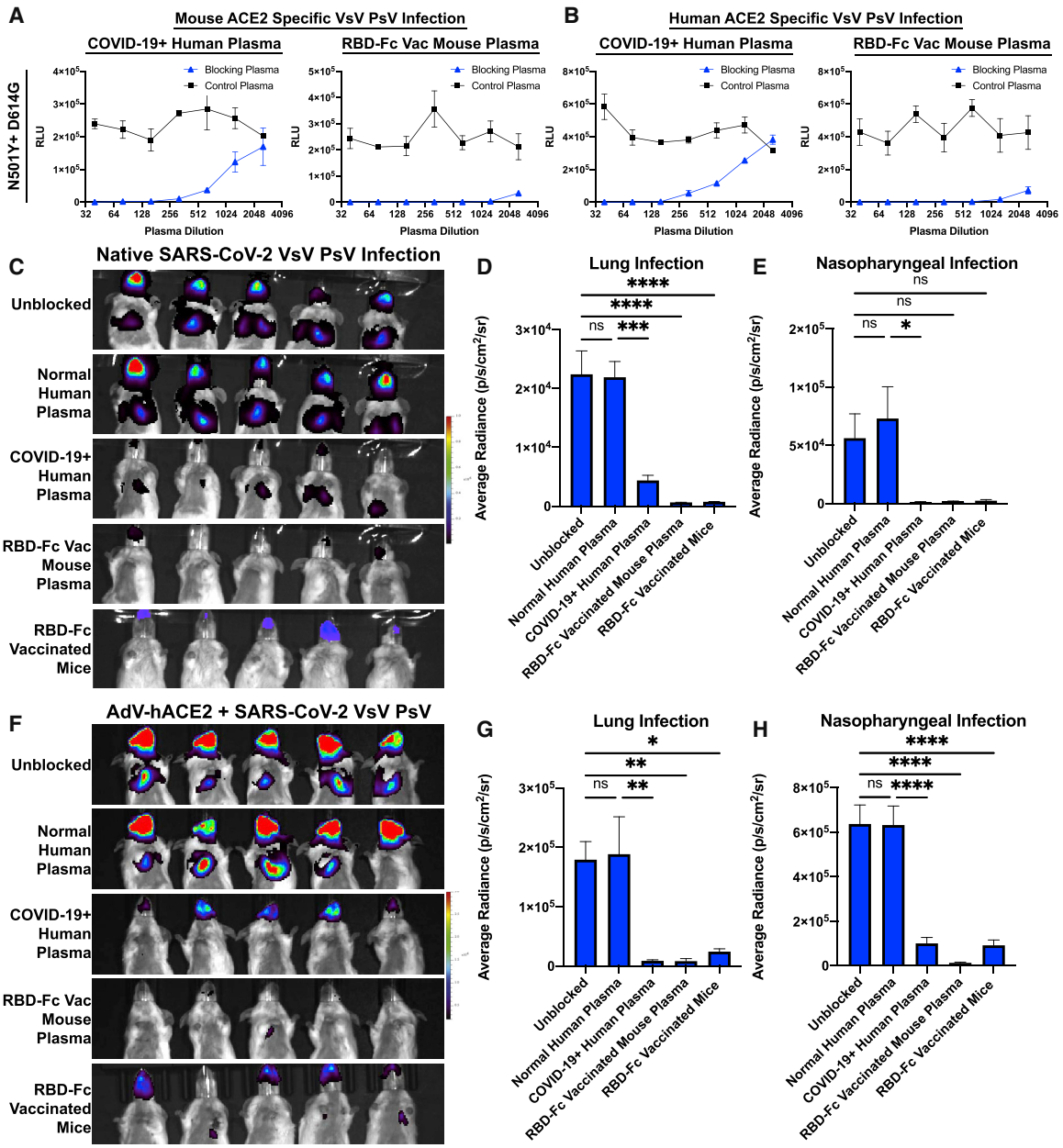

Figure 2. Application of SARS-CoV-2 N501Y variant VSV-based murine model to intervention studies

(A and B) *In vitro* neutralization of SARS-CoV-2 VSV PsV infection on (A) mACE2+ or hACE2+ (B) 293 cells. Luciferase-expressing N501Y + D614G PsVs were preincubated with COVID-19+ plasma, RBD-Fc-vaccinated mouse plasma, or species-matched control plasma at the indicated dilutions on the x axis over a 2-fold dilution range. The plasma-PsV mixture was then added to mACE2+ 293 cells. 48 h later, cells were lysed and analyzed for luciferase activity as a measure of infection via GloMax. The left panels show blocking with COVID-19+ human plasma or control COVID19− human plasma. The right panels show blocking of infection with RBD-Fc vaccinated mouse plasma or naive mouse plasma (n = 3).

(C) *In vivo* blocking of SARS-CoV-2 VSV PsV infection. Prior to infection of BALB/c mice as in Figure 1, mice were administered normal human plasma, COVID-19+ human plasma, or RBD-Fc-vaccinated mouse plasma or vaccinated with RBD-Fc protein. All mice were administered anti-IFNAR1 24 h prior to infection with N501Y + D614G SARS-CoV-2 VSV PsVs intranasally. 24 h later, mice were administered 80 μg of D-luciferin intranasally and 100 μg intravenously and then imaged via IVIS for 5 min with an open emission filter. All groups were set to the same scale during image processing.

(D and E) Quantification of signal in the lungs (D) and nasopharyngeal passage (E) of mice infected with N501Y + D614G SARS-CoV-2 VSV PsVs and blocked or vaccinated as indicated (n = 5).

(F) *In vivo* blocking of SARS-CoV-2 VSV PsV infection following AdV5-hACE2 transduction intranasally. Mice were treated with plasma transfer or vaccination identically as in (C), but 4 days prior to PsV infection, mice were transduced intranasally with AdV5-hACE2 to achieve hACE2 expression in the airway. 24 h after challenge, mice were administered D-luciferin as in (C) and imaged.

(legend continued on next page)

using this method allowed us to make fair comparisons and control for the heightened primary infection levels seen with N501Y + K417N + E484K + D614G compared with N501Y + D614G PsVs (Figures 3C–3E). Infection in the nasopharynx is shown because immunity in this tissue location would likely be clinically crucial for reinfection susceptibility. Primary and secondary infection with N501Y + D614G PsVs yielded significantly lower RLUs upon rechallenge (Figures 3F–3H). However, primary infection with N501Y + D614G and secondary infection with South Africa N501Y + K417N + E484K + D614G PsVs yielded no significant reduction in RLUs (Figures 3F–3H), suggesting that N501Y + K417N + E484K + D614G may have escaped antibodies generated during the primary infection. Analysis of plasma collected from mice in each treatment arm revealed that anti-spike antibody responses were generated in the primary response of mice, and robust rechallenge antibody responses were observed, suggesting that the reinfection phenomenon was immune mediated (Figures 3I–3K). This supports that infectivity and potential susceptibility to reinfection of emerging spike variants can be explored using our *in vivo* model system.

Immune escape of the South Africa variant from human COVID-19+ antibodies and antibodies from vaccinated individuals *in vitro*

The heightened infectivity and rechallenge susceptibility mediated by K417N + E484K mutations prompted us to explore their effects on antibody-mediated neutralization, which is of the utmost importance for formulating effective public health strategies to combat the spread of SARS-CoV-2 variants (Collier et al., 2021; Jangra et al., 2021; Mahase, 2021; Muik et al., 2021; Wang et al., 2021c). To accomplish this, two cohorts of individuals with SARS-CoV-2-specific antibodies were examined. The first group was a cohort of 45 samples drawn randomly from a pool of potential convalescent plasma donors who had molecularly confirmed SARS-CoV-2 infection. The pool consisted mostly of individuals with mild to moderate COVID-19, with less than 10% requiring hospitalization. Plasma samples were collected approximately 43 days after confirmation of infection (Heaney et al., 2021; Klein et al., 2020; Patel et al., 2021). The second cohort of 15 serum samples was collected from a pool of uninfected volunteer hospital workers at least 14 days following administration of the second dose of the Moderna or Pfizer-BioNTech COVID-19 vaccine who had a documented SARS-CoV-2 immunoglobulin G (IgG) response to the vaccine. COVID-19+ samples were stratified into low-, mid-, and high-tier antibody groups based on their reported antibody neutralization titer and their median fluorescence intensity (MFI) following staining of SARS-CoV-2 spike+ cells (Figure S5D; Heaney et al., 2021; Klein et al., 2020; Patel et al., 2021). Vaccinated individuals were stratified into low- or high-tier antibody groups based on MFI after staining spike+ cells (Figure S5E).

First we explored the ability of plasma samples from each cohort to neutralize infection of N501Y + D614G, Los Angeles N501Y + L452R + D614G, and South Africa N501Y + K417N+ E484K + D614G PsVs on hACE2+ 293 cells. Representative neutralization curves for each individual and titer group are shown for reference (Figures 4A–4E). We found significant dose-dependent neutralization of SARS-CoV-2 VSV PsVs in the COVID-19+ and vaccinated groups (Figures 4F–4H). This trend held for all 3 SARS-CoV-2 PsVs and was confirmed when analyzing neutralization ability versus antibody level (Figures 4I–4K). Reciprocal log of half-maximal inhibitory concentration($\log_{10}IC_{50}$) values for high-tier COVID-19 individuals and high-tier vaccinated individuals were comparable (Figures 4F–4H), suggesting that both possess high neutralization ability. When examining the ability of COVID-19+ and vaccinated individuals to neutralize South Africa N501Y + K417N + E484K + D614G VSV PsVs compared with N501Y + D614G VSV PsVs, markedly lower reciprocal $\log_{10}IC_{50}$ values were noted for the South Africa N501Y + K417N + E484K + D614G variant, suggesting that it was not neutralized as efficiently as the N501Y + D614G variant (Figure 4G). This decrease in neutralization ability was not observed for the Los Angeles N501Y + L452R + D614G variant (Figure 4H). Individual neutralization curves for each plasma sample and variant PsV combination were also determined (Figure S4). Similar findings were observed for murine SARS-CoV-2 antisera (Figures S6A–S6F).

SARS-CoV-2 escape variant-binding ability and isotypes of antibodies found in human COVID-19+ and vaccinated individuals

We wanted to explore factors beyond titer that could be contributing mechanistically to the immune escape seen with South Africa N501Y + K417N + E484K + D614G PsV in the presence of COVID-19+ and vaccinated individual plasma samples. First we measured IgG antibody levels that specifically bind the WT RBD versus the N501Y + K417N + E484K + D614G variant RBD. This varies from total anti-spike antibodies because RBD-directed antibodies would contribute significantly more to the observed differential neutralization and immune escape. Although the same titer trends remained for WT IgG RBD-directed responses compared with anti-spike, significant ablation of binding was observed for IgGs against the N501Y + K417N + E484K + D614G RBD (Figure 4L; Figure S5A). This trend appeared to be even stronger for low- to mid-tier groups in COVID-19+ individuals. High-tier COVID-19+ and vaccinated individual plasma samples still suffered from a decrease in N501Y + K417N + E484K + D614G RBD IgG levels, but it was not as pronounced. We extended this study to anti-SARS-CoV-2 RBD IgM (Figures 4L and 4M; Figure S5B) and IgA (Figures 4L and 4N; Figure S5C) titers. Although present, less pronounced anti-WT RBD levels were seen between each tier group for IgM and IgA. Interestingly, a clear trend was not present between WT or N501Y + K417N + E484K + D614G RBD IgM or IgA levels compared with IgG levels, where a clear decrease was observed. These findings suggest that the

(G and H) Quantification of signal in the lungs (G) and nasopharyngeal passage (H) of mice transduced with AdV5-hACE2, infected with N501Y + D614G SARS-CoV-2 VSV PsVs, and blocked or vaccinated as indicated (n = 5).

Experiments were performed in technical triplicates (A and B) or 5 biological replicates (C–H). Mean ± SEM is shown. *, **, and *** indicate p values less than 0.05, 0.01, and 0.001, respectively; N.S., not significant.

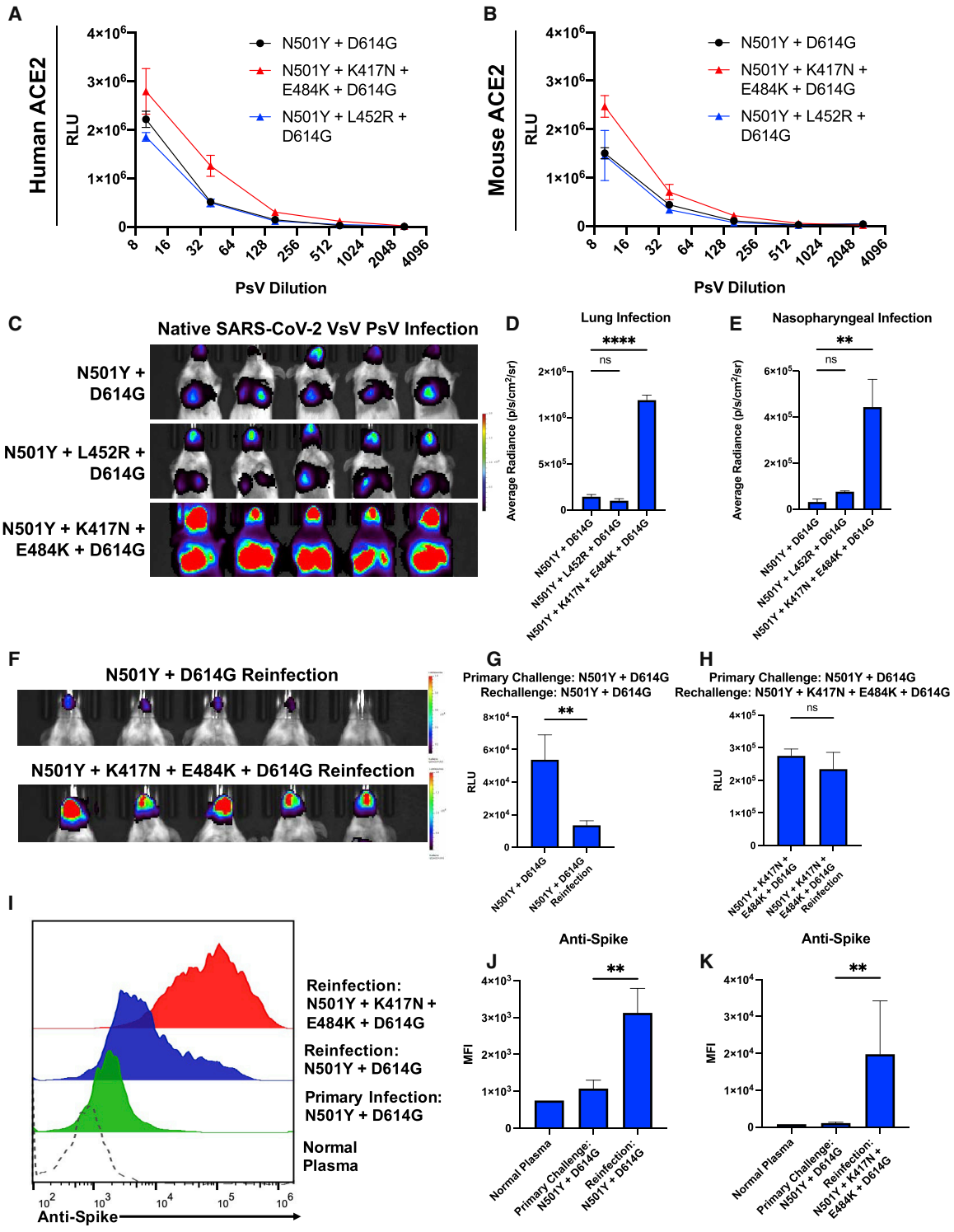

Figure 3. Infectivity and reinfection potential of L452R and K417N + E484K spike mutation bearing SARS-CoV-2 PsVs *in vivo*

(A and B) *In vitro* infection assay of VSV PsVs, including N501Y + D614G, N501Y + L452R + D614G, and N501Y + K417N + E484K + D614G, on 293 cells transfected with human ACE2 (A) or mouse ACE2 (B). All PsVs were normalized to the total amount of SARS-CoV-2 S protein by western blot, titrated across a 2-fold range as indicated on the x axis, and then added to cells that were seeded 24 h prior to infection. 48 h later, cells were lysed and analyzed for luciferase activity via GloMax as a readout of infection level (n = 3).

(legend continued on next page)

N501Y + K417N + E484K + D614G variant may have immune escape capabilities to natural and vaccine-induced anti-COVID-19 immunity, with differential effects exerted by WT versus variant-binding IgGs but not IgMs or IgAs.

In vivo escape of the South Africa variant from plasma of human COVID-19+ and vaccinated individuals

Next, we employed our *in vivo* system to further investigate this escape phenomenon. As in Figure 2, mice received a transfer of human plasma samples, including the COVID-19+ and vaccinated groups, and then challenged with the indicated variant SARS-CoV-2 VSV PsV. Three plasma samples from each COVID-19+ tier and five samples from each vaccinated tier were transferred to three mice for each VSV PsV infection. We observed antibody dose-dependent neutralization of all three variant VSV PsVs tested (Figures 5A–5F). Mice receiving high-tier COVID-19+ or vaccinated plasma samples did not display detectable lung infection and only exhibited extremely low-level nasopharyngeal infection (Figure 5; Figures S6G–S6I). In contrast, mice receiving low-level antibody plasma samples were able to neutralize a significant amount of lung infection but not nasopharyngeal infection. This has potential clinical correlation because individuals with a history of COVID-19 infection or vaccination are known to develop less severe disease upon reinfection, suggesting the ability of our system to model this clinical phenomenon. Similar to *in vitro*, partial immune escape was observed for the South Africa N501Y + K417N + E484K + D614G variant (Figures 5E and 5F) compared with N501Y + D614G (Figures 5A and 5B). This is especially striking when examining the ability of high-tier COVID-19+ and vaccinated plasma samples to control the South Africa N501Y + K417N + E484K + D614G variant.

Assessment of the India variant using SARS-CoV-2 PsVs

Finally, given the severe outbreak of COVID-19 in India and the presence of a variant possessing a unique combination of mutations, including N501Y + L452R + K417N + E484Q + D614G (kappa variant), we sought to explore this variant in our system. *In vitro* infection assays of hACE2+ cells revealed that PsVs carrying these mutations were significantly infectious but not quite to the levels observed for the N501Y + K417N + E484K + D614G variant (Figure 6A). When applying these variants *in vivo*, a similar phenomenon was observed; the N501Y + L452R + K417N + E484Q + D614G variant PsVs were highly infective, but significantly higher infection was observed in the nasopharynx, but not lungs, of mice infected with the N501Y + K417N + E484K + D614G variant (Figures 6B–6D). We also explored the ability of COVID-19+ plasma to neutralize the N501Y + L452R + K417N + E484Q + D614G variant. Immune escape of the India variant was observed for low-tier COVID-19+ plasma, similar to that observed with the South Africa variant (Figures 6E–6H).

DISCUSSION

In this study, we demonstrate that the N501Y SARS-CoV-2 variant permits enhanced hACE2 binding, species switch, and subsequent high-level VSV PsV infection in unmodified laboratory mice. Our study also supports the possibility that rodents could become infected with variants containing N501Y (Gu et al., 2020). This platform can be used readily to model SARS-CoV-2 infection in mice with or without hACE2. When exploring emerging COVID-19 variants, high-level infectivity was observed for the South Africa and India variants, but infectivity was not significantly higher for the Los Angeles variant. In addition to heightened infectivity, antibody escape from previous murine infection or transfer with COVID-19+ and vaccinated human plasma was observed *in vitro* and in mice infected with PsVs carrying crucial mutations in the South Africa variant.

Use of VSV PsVs permits strong infection in the nasopharynx and lungs of animals, anatomically closely mimicking human infection. Although other groups have explored adaptation of viable SARS-CoV-2 for murine infection studies (Gu et al., 2020), there are distinct advantages to using viable versus pseudotyped SARS-CoV-2 as in our study. PsVs can be employed under ABSL-2 conditions, which limits occupational hazards and potential environmental leaks. In addition, PsVs are easy to engineer and incorporate emerging mutations with common molecular biology techniques, unlike engineering viable SARS-CoV-2, which requires special equipment and additional time. PsVs can also be used to study reinfection dynamics and immunologic interplay. Our study demonstrated that N501Y + K417N + E484K + D614G PsVs can escape antibodies

(C) *In vivo* infectivity of VSV PsVs in BALB/c mice. 24 h prior to infection, mice were administered anti-IFNAR1 as described, challenged with the indicated VSV PsVs intranasally, followed by a PBS wash. 24 h later, mice were administered 80 μg of D-luciferin intranasally and 100 μg intravenously and then imaged via IVIS for 5 min with an open emission filter. All groups were set to the same scale during image processing.

(D and E) Quantification of bioluminescence activity in the lungs (D) and nasopharynx (E) of mice infected with the indicated PsVs. Shown is reinfection modeling of SARS-CoV-2 PsVs. Mice were first challenged with N501Y + D614G VSV PsVs. 2 weeks later, mice were rechallenged with N501Y + D614G or N501Y + K417N + E484K + D614G PsVs.

(F) Image of mice following reinfection with the indicated PsVs as in (C). The scale was set based on primary infection with N501Y + D614G or N501Y + K417N + E484K + D614G PsVs because this would indicate the predicted level of infection without preexisting immunity.

(G) Quantification of nasopharyngeal signal in mice following primary infection with N501Y + D614G and then N501Y + D614G rechallenge compared with N501Y + D614G reference infection.

(H) Quantification of nasopharyngeal signal in mice following primary infection with N501Y + D614G and then N501Y + K417N + E484K + D614G rechallenge compared with N501Y + K417N + E484K + D614G reference infection.

(I–K) Plasma anti-SARS-CoV-2 spike levels represented via histogram (I) or bar graphs (J and K) in infection groups, including naive mice (normal plasma), primary infection with N501Y + D614G, reinfection with N501Y + D614G, and reinfection with N501Y + K417N + E484K + D614G. Plasma was collected 2 weeks after primary infection or 2 weeks after reinfection.

Experiments were performed in technical triplicates (A and B) or 5 biological replicates (C–K). Mean ± SEM is shown. *, **, and *** indicate p values less than 0.05, 0.01, and 0.001, respectively; N.S., not significant.

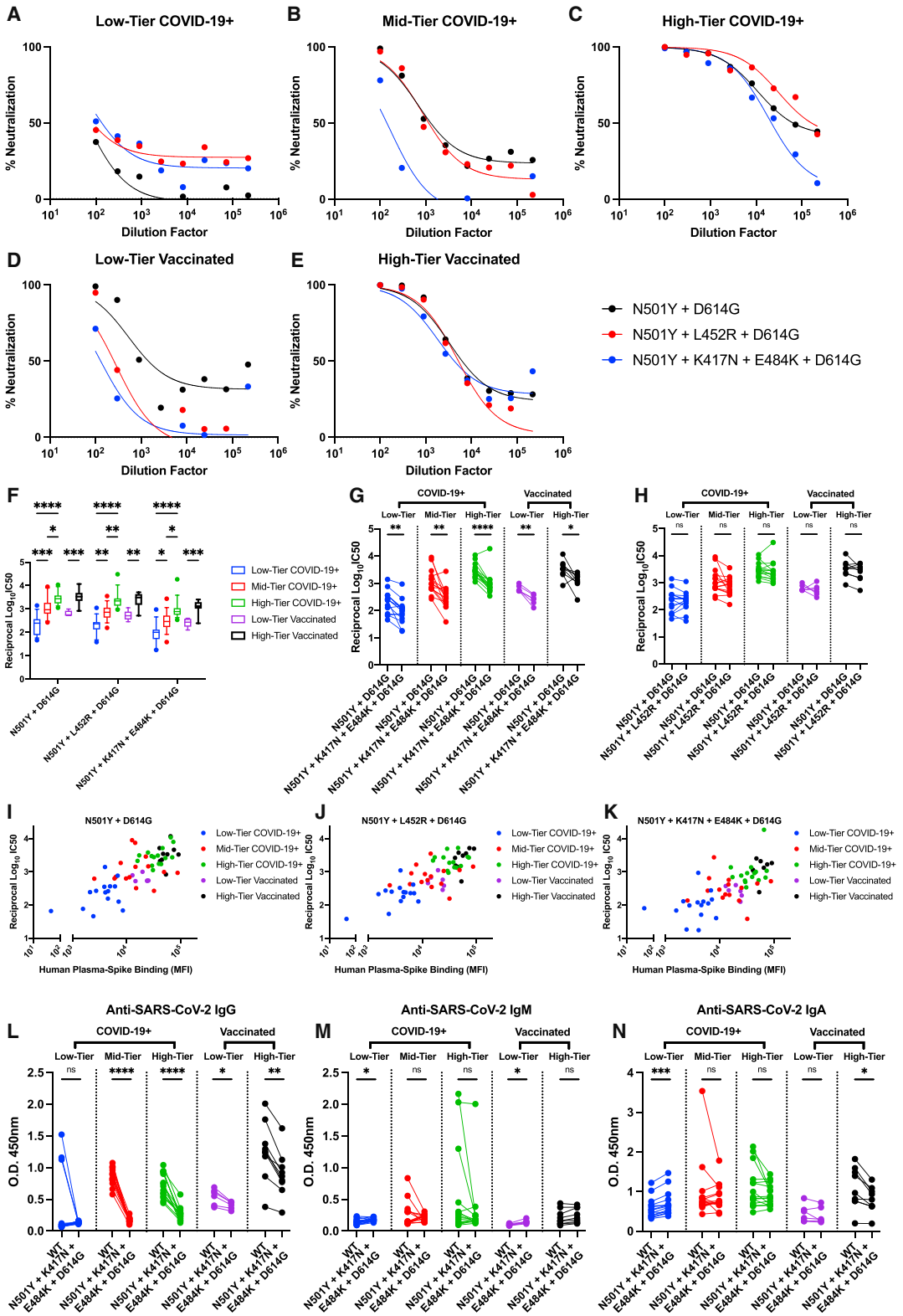

(legend on next page)

generated by N501Y + D614G PsVs, allowing successful secondary infection in mice. As the pandemic continues, SARS-CoV-2 variants with greater immune escape potential, such as those modeled using the N501Y + K417N + E484K + D614G variant PsV, have dominated new COVID-19 cases globally. In future murine PsV reinfection studies, the N501Y + K417N + E484K + D614G PsV could be used for primary infection, followed by other emerging variant PsVs. This would allow us to further our understanding of immunity to primary SARS-CoV-2 infection and susceptibility to reinfection in the current SARS-CoV-2 variant landscape. It is unclear what the challenges would be to sequentially reinfect mice with viable SARS-CoV-2. Finally, PsVs carrying reporter plasmids such as in our system allow seamless measurement of infection using optical imaging. Conversely, the downside of PsV application *in vivo* is that they limit the ability to study tissue damage and murine transmission, which, theoretically, could be studied using viable SARS-CoV-2.

There are many potential explanations for the lower infectivity observed for the Los Angeles variant, including the theory that L452R drives enhanced transmissibility but not necessarily infectivity. This is further supported by our study regarding infectivity of PsVs incorporating mutations found in the India variant because the L452R mutation was also present and did not mediate enhancement of infection compared with the South Africa variant PsV.

Regarding the immune escape observed in our experiments, many other groups have begun to explore this phenomenon in the context of different SARS-CoV-2 variants with plasma from COVID-19+ and vaccinated individuals (Cele et al., 2021; Collier et al., 2021; Muik et al., 2021; Wang et al., 2021a, 2021b). Although our study draws similar conclusions regarding the dose dependency of immune escape to emerging spike variants, we are the first to do so *in vivo*, providing additional anatomical context. When exploring the ability of antibodies in both groups of individuals to bind the WT RBD versus N501Y + K417N + E484K + D614G variant RBD, we observed significant ablation of binding to the variant, particularly for IgGs. This likely explains the dose dependency we observed. As overall SARS-CoV-2 titers decrease, so do titers capable of binding the variant. For individuals in the low-tier groups, variant binding IgG levels were more than two times lower. It is easy to imagine how this would lead to disappearance of anti-variant RBD antibodies while anti-RBD titers could still remain. Perhaps this ratio of WT versus variant binding antibodies would change over time in people as antibodies continue to evolve in the presence of antigen (Gaebler et al., 2021). In theory, this could also be easy to explore in our *in vivo* system and could be expanded to understand antibody evolution in the presence of different variant RBDs at different times sequentially.

In our study, we detected plasma IgM and IgA anti-SARS-CoV-2 levels, which aligns with other studies documenting that IgA may dominate the early-phase response to SARS-CoV-2 (Sterlin et al., 2021). It was interesting that there was no significant difference in IgAs' and IgMs' ability to bind the WT versus N501Y + K417N + E484K + D614G variant RBD. This could be explained by differences in somatic hypermutation kinetics and timing of B cell class switching to these isotypes. The neutralization ability of polyclonal IgG, IgM, and IgA anti-SARS-CoV-2 antibody pools from COVID-19+ and vaccinated individuals could be delineated further *in vivo* using our system in future studies.

A unique benefit of our system compared with *in vitro* approaches to measuring SARS-CoV-2 variant infectivity and immune escape is the anatomical context mice provide. It is known that individuals with preexisting SARS-CoV-2 immunity because of having received COVID-19 vaccines or being infected with COVID-19 generally develop less severe disease in the case of reinfection, especially those that have high-titer antibodies. In our study, mice receiving high-tier plasma samples were only infected by variant PsVs in the nasopharynx and not in the lungs. It is well understood that severe lung infection and associated pathologies are a major factor contributing to the virulence of SARS-CoV-2, especially when considering variants. This phenomenon would not be appreciable *in vitro*. Our model system serves as a robust "plug and play" *in vivo* technique to model clinical factors affecting human SARS-CoV-2 variant infectivity and control.

Limitations of study

Here we demonstrate the ability of N501Y-bearing SARS-CoV-2 variants to model COVID-19 in common laboratory mouse strains.

Figure 4. Effect of L452R and K417N + E484K spike mutations on the ability of antibodies from COVID-19+ or vaccinated individuals to bind and neutralize SARS-CoV-2

Shown is *in vitro* neutralization of variant SARS-CoV-2 VSV PsV infection on human ACE2+ 293 cells. Luciferase-expressing PsVs, including N501Y + D614G, N501Y + L452R + D614G, and N501Y + K417N + E484K + D614G, were preincubated with 45 COVID-19+ plasma samples, 15 COVID-19-vaccinated plasma samples, or 4 control plasma samples over a 3-fold dilution range. Samples were stratified based on antibody levels, as described, into low, mid, and high tier for COVID-19+ individuals and low or high tier for vaccinated individuals. The plasma-PsV mixture was then added to seeded hACE2+ 293 cells. 48 h later, cells were lysed and analyzed for luciferase activity as a measure of infection via GloMax.

(A–E) Representative neutralization curves for the indicated COVID-19+ or vaccinated tier groups against the N501Y + D614G, N501Y + L452R + D614G, or N501Y + K417N + E484K + D614G PsVs.

(F) Neutralization ability as reciprocal $\log_{10}IC_{50}$ of the indicated human plasma samples mixed with the indicated PsVs. Samples were normalized to control plasma prior to neutralization curve fit and reciprocal $\log_{10}IC_{50}$ determination.

(G and H) Comparison of neutralization ability of each indicated COVID-19+ or vaccinated group between (G) N501Y + K417N + E484K + D614G and N501Y + D614G PsV infection or (H) N501Y + L452R + D614G and N501Y + D614G PsV infection.

(I–K) Comparison of reciprocal $\log_{10}IC_{50}$ and MFI of spike-plasma binding. Plasma samples were incubated with hACE2+ cells, stained with an anti-human IgG secondary, and then analyzed by flow cytometry to determine antibody levels. MFI for each plasma samples was graphed against reciprocal $\log_{10}IC_{50}$ for each plasma incubated with (I) N501Y + D614G, (J) N501Y + L452R + D614G, and (K) N501Y + K417N + E484K + D614G VSV PsVs.

(L–N) WT versus N501Y + K417N + E484K + D614G RBD-specific (L) IgG, (M) IgM, and (N) IgA antibody levels from COVID-19+ or vaccinated individuals stratified by anti-SARS-CoV-2 spike tier groups.

All experiments were performed in 4–15 biological replicates and technical duplicates. *, **, and *** indicate p values less than 0.05, 0.01, and 0.001, respectively; N.S., not significant.

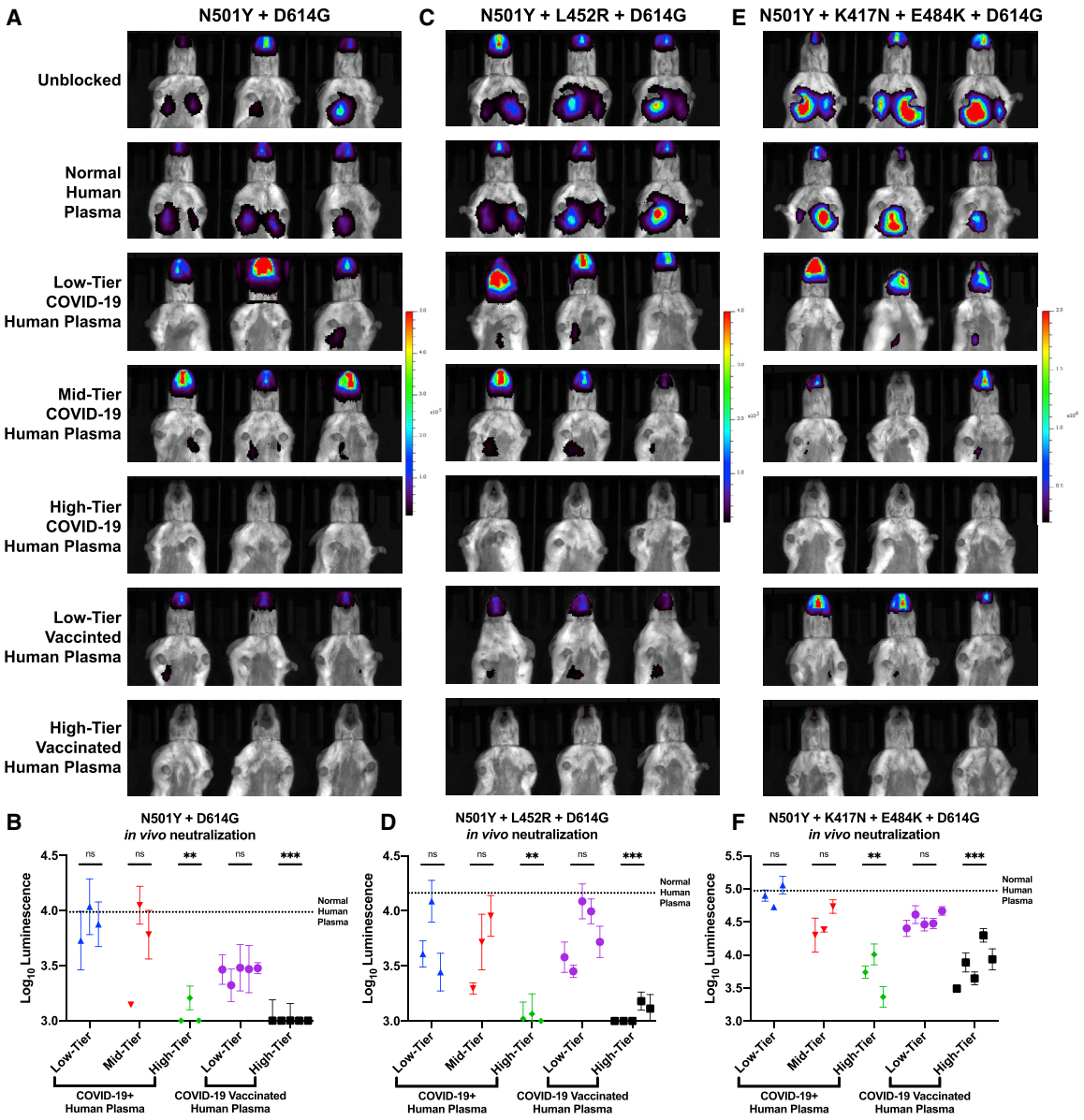

Figure 5. *In vivo* neutralization of L452R and K417N + E484K variant PsVs by COVID-19+ or vaccinated plasma

(A–F) *In vivo* neutralization of SARS-CoV-2 VSV PsVs carrying emerging L452R and K417N + E484K spike mutations by COVID-19+ or vaccinated human plasma samples. Prior to infection, BALB/c mice were administered normal human plasma, COVID-19+ human plasma (3 plasma samples per tier group), or vaccinated human plasma samples (5 plasma samples per tier group). All mice were administered anti-IFNAR1 24 h prior to infection with N501Y + D614G, N501Y + L452R + D614G, or N501Y + K417N + E484K + D614G SARS-CoV-2 VSV PsVs intranasally. 24 h later, mice were administered 80 μg of D-luciferin intranasally and 100 μg intravenously and then imaged via IVIS for 5 min with an open emission filter. All groups were set to the same scale during image processing for each different VSV PsV. Shown are representative image and luminescence values for mice infected with (A and B) N501Y + D614G, (C and D) N501Y + L452R + D614G, and (E and F) N501Y + K417N + E484K + D614G VSV PsVs and transferred with the indicated human plasma samples. Each dot represents an average of 3 mice. The bottom of the scale indicates background luminescence, and a dotted line represents luminescence following transfer with normal human plasma. The p values were calculated between the indicated experimental groups and the luminescence signal of normal human plasma. Experiments were performed in biological triplicates. Mean ± SEM is shown. *, **, and *** indicate p values less than 0.05, 0.01, and 0.001, respectively; N.S., not significant.

Although numerous areas for further research are explored in our Discussion, additional limitations of our studied that should be considered alongside our work are highlighted here.

Although we show that the N501Y variant drives a species switch of SARS-CoV-2 PsVs to the mouse (Figure 1), we are not the first group to show the importance of this point mutation. It was first demonstrated in an *in vivo* passaged preparation of SARS-CoV-2 that possessed murine tropism and carried the N501Y mutation (Gu et al., 2020). Although additional studies elaborated the importance of the N501Y mutation (Cele et al.,

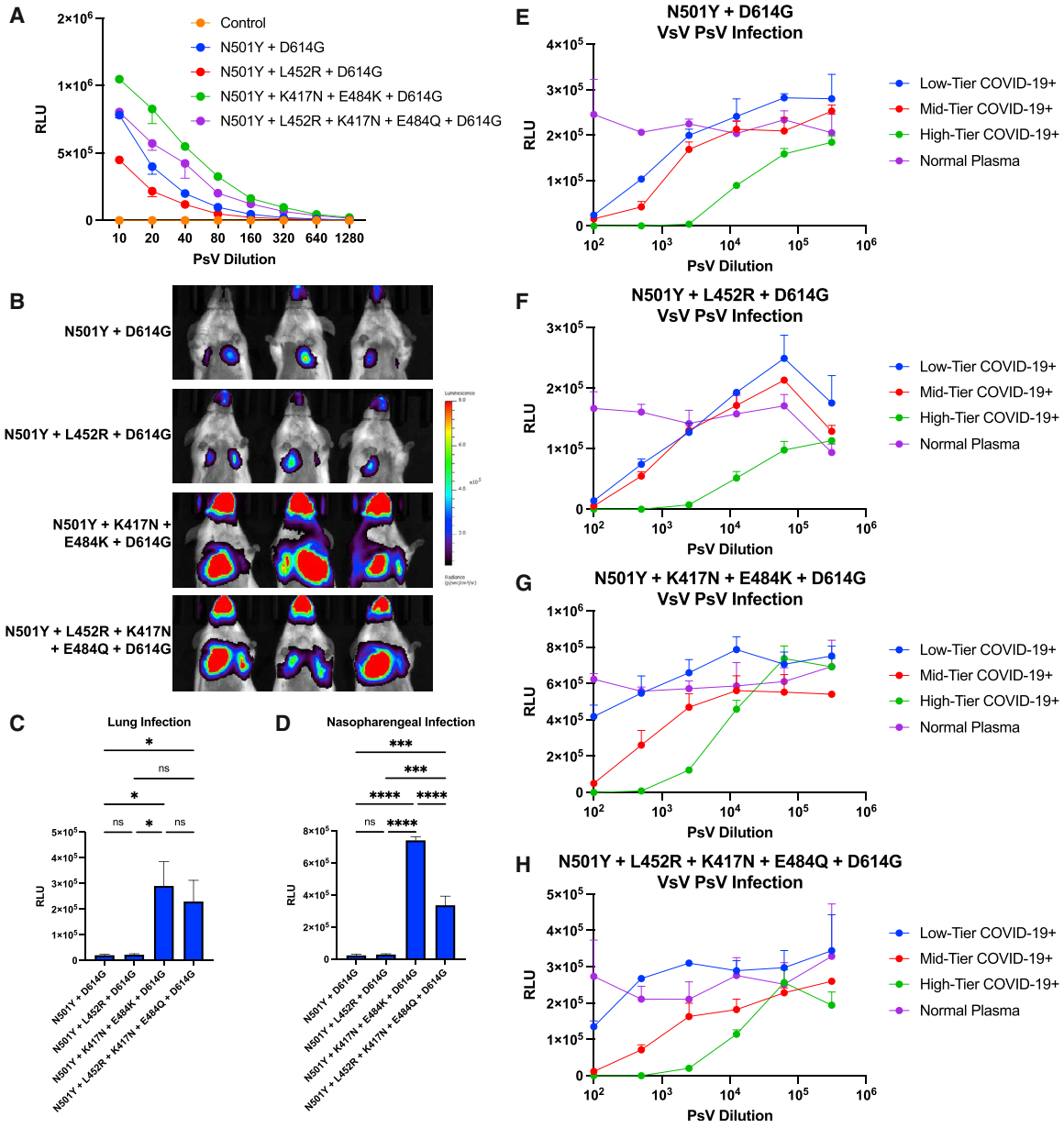

Figure 6. Infectivity and immune escape potential of the N501Y + L452R + K417 + E484Q + D614G India variant

(A) *In vitro* infectivity of SARS-CoV-2 PsVs, including N501Y + D614G, N501Y + L452R + D614G, N501Y + K417N + E484K + D614G, and N501Y + L452R + K417N + E484Q + D614G, on 293 cells transfected with human ACE2. All PsVs were normalized to the total amount of SARS-CoV-2 S protein by western blot, titrated across a 2-fold range as indicated on the x axis, and then added to cells that were seeded 24 h prior to infection. 48 h later, cells were lysed and analyzed for luciferase activity via GloMax.

(B) *In vivo* infectivity of VSV PsVs in BALB/c mice. 24 h prior to infection, mice were administered anti-IFNAR1 as described, challenged with the indicated VSV PsVs intranasally, followed by a PBS wash. 24 h later, mice were administered 80 μg of D-luciferin intranasally and 100 μg intravenously and then imaged via IVIS for 5 min with an open emission filter. All groups were set to the same scale during image processing.

(C and D) Quantification of bioluminescence activity in the lungs (C) and nasopharynx (D) of mice infected with the indicated PsVs.

(E–H) *In vitro* neutralization of variant SARS-CoV-2 VSV PsV infection on human ACE2+ 293 cells. Luciferase-expressing PsVs, including (E) N501Y + D614G, (F) N501Y + L452R + D614G, (G) N501Y + K417N + E484K + D614G, and (H) N501Y + L452R + K417N + E484Q + D614G, were preincubated with serially diluted low-, mid-, or high-tier COVID-19+ plasma prior to infection. RLUs at the indicated dilutions are shown.

Experiments were performed in technical triplicates (A) or biological triplicates (B–H). Mean ± SEM is shown. *, **, and *** indicate p values less than 0.05, 0.01, and 0.001, respectively; N.S., not significant.

2021; Roy Wong et al., 2021), we are the first to use N501Y to model emerging SARS-CoV-2 variants *in vivo*.

In our study, Lenti- or VSV-based SARS-CoV-2 PsVs are used to model COVID-19 (Figure 1). We demonstrate that VSV-based PsVs are significantly more infective and use them for our detailed *in vivo* studies (Figures 1, 2, 3, 4, 5, and 6). The biggest advantage of using PsVs is that they allow experiments to be conducted under ABSL-2 conditions, significantly reducing cost and occupational hazards. ABSL-2 conditions also make it simple for other groups to reproduce our system in various lab environments. However, this system brings with it many limitations, including lack of spread, a single round of infection, and inability to model clinical pathogenesis of SARS-CoV-2. Accordingly, our data (Figures 4, 5, and 6) regarding reinfection and neutralization can only be interpreted in the context of a single round of PsV infection, not true viral replication, and host-to-host transmission.

In our experiments involving human plasma transfer to mice to study *in vivo* PsV neutralization, plasma was always transferred intranasally. This route of administration was chosen because it would allow minimal volumes of human plasma to be transferred to the animals, which would limit off-target inflammation because of the presence of foreign plasma. It would also theoretically bypass any issues with human antibodies translocating from the murine circulation to the airway. It is important to keep this in mind because intranasal plasma administration is artificial in nature; plasma would only be expected to be found in vessels. These limitations should be considered when interpreting the work in this study.

STAR★METHODS

Detailed methods are provided in the online version of this paper and include the following:

- KEY RESOURCES TABLE
- RESOURCE AVAILABILITY
  - Lead contact
  - Materials availability
  - Data and code availability
- EXPERIMENTAL MODEL AND SUBJECT DETAILS
  - Animals
  - Human samples
  - Cell lines
- METHOD DETAILS
  - Plasmids for PsV prep
  - Generation of HIV-I SARS-CoV-2 spike PsVs
  - Generation of VsV SARS-CoV-2 spike PsVs
  - Protein production and purification
  - Antibody quantification by flow cytometry
  - Antibody characterization by ELISA
  - Mouse experiments
  - Microscopy
  - RBD and ACE2 structure visualization
  - RBD and RBD-Fc protein quality assessment
  - PsV quantification
  - Binding affinity assay
  - *In vitro* infection assay
  - *In vitro* blocking assay
- QUANTIFICATION AND STATISTICAL ANALYSIS

SUPPLEMENTAL INFORMATION

Supplemental information can be found online at https://doi.org/10.1016/j.celrep.2021.109838.

ACKNOWLEDGMENTS

The authors would like to acknowledge Christopher Carter Polston and Louise Ferrall for providing administrative assistance. In addition, we would like to thank Dr. Robert Bloch and Dr. Yinghua Zhang of the biosensor core at the University of Maryland School of Medicine for support and services while completing our surface plasmon resonance experiments. This study was supported by an NIH-supported research grant (5P50CA098252). B.L. is a recipient of an NIH-supported career development fellowship (5F31CA236051). The graphical abstract was generated using BioRender.

AUTHOR CONTRIBUTIONS

Conception and design, B.L., R.B.S.R., T.C.W., and C.-F.H.; performance of experiments, B.L., Y.J.K., J.L., S.-H.T., Y.C.T., L.H., and G.C.; analysis and interpretation of data, B.L., Y.J.K., J.L., and C.-F.H.; writing, review, and/or revision of the manuscript, B.L., Y.J.K., J.L., E.E., E.M.B., A.A.R.T., A.M.M., E.J.D., R.B.S.R., T.C.W., and C.-F.H.; study supervision, R.B.S.R.R., T.C.W., and C.-F.H.

DECLARATION OF INTERESTS

The authors declare no competing interests.

INCLUSION AND DIVERSITY

One or more of the authors of this paper self-identifies as an underrepresented ethnic minority in science. While citing references scientifically relevant for this work, we also actively worked to promote gender balance in our reference list.

Received: May 27, 2021
Revised: August 30, 2021
Accepted: September 23, 2021
Published: October 5, 2021

REFERENCES

Brooke, G.N., and Prischi, F. (2020). Structural and functional modelling of SARS-CoV-2 entry in animal models. Sci. Rep. *10*, 15917.

Buck, C.B., Pastrana, D.V., Lowy, D.R., and Schiller, J.T. (2004). Efficient intracellular assembly of papillomaviral vectors. J. Virol. *78*, 751–757.

CDC (2021a). Science Brief: COVID-19 Vaccines and Vaccination, https://www.cdc.gov/coronavirus/2019-ncov/science/science-briefs/fully-vaccinated-people.html.

CDC (2021b). https://www.cdc.gov/coronavirus/2019-ncov/science/science-briefs/scientific-brief-emerging-variants.html.

Cele, S., Gazy, I., Jackson, L., Hwa, S.H., Tegally, H., Lustig, G., Giandhari, J., Pillay, S., Wilkinson, E., Naidoo, Y., et al.; Network for Genomic Surveillance in South Africa; COMMIT-KZN Team (2021). Escape of SARS-CoV-2 501Y.V2 from neutralization by convalescent plasma. Nature *593*, 142–146.

Collier, D.A., De Marco, A., Ferreira, I.A.T.M., Meng, B., Datir, R.P., Walls, A.C., Kemp, S.A., Bassi, J., Pinto, D., Silacci-Fregni, C., et al.; CITIID-NIHR BioResource COVID-19 Collaboration; COVID-19 Genomics UK (COG-UK) Consortium (2021). Sensitivity of SARS-CoV-2 B.1.1.7 to mRNA vaccine-elicited antibodies. Nature *593*, 136–141.

Forni, G., and Mantovani, A.; COVID-19 Commission of Accademia Nazionale dei Lincei, Rome (2021). COVID-19 vaccines: where we stand and challenges ahead. Cell Death Differ. *28*, 626–639.

Fratev, F. (2020). The N501Y and K417N mutations in the spike protein of SARS-CoV-2 alter the interactions with both hACE2 and human derived antibody: A Free energy of perturbation study. bioRxiv. https://doi.org/10.1101/2020.12.23.424283.

Gaebler, C., Wang, Z., Lorenzi, J.C.C., Muecksch, F., Finkin, S., Tokuyama, M., Cho, A., Jankovic, M., Schaefer-Babajew, D., Oliveira, T.Y., et al. (2021). Evolution of antibody immunity to SARS-CoV-2. Nature *591*, 639–644.

Giroglou, T., Cinatl, J., Jr., Rabenau, H., Drosten, C., Schwalbe, H., Doerr, H.W., and von Laer, D. (2004). Retroviral vectors pseudotyped with severe acute respiratory syndrome coronavirus S protein. J. Virol. *78*, 9007–9015.

Gu, H., Chen, Q., Yang, G., He, L., Fan, H., Deng, Y.Q., Wang, Y., Teng, Y., Zhao, Z., Cui, Y., et al. (2020). Adaptation of SARS-CoV-2 in BALB/c mice for testing vaccine efficacy. Science *369*, 1603–1607.

Hansen, C.H., Michlmayr, D., Gubbels, S.M., Mølbak, K., and Ethelberg, S. (2021). Assessment of protection against reinfection with SARS-CoV-2 among 4 million PCR-tested individuals in Denmark in 2020: a population-level observational study. Lancet *397*, 1204–1212.

Harrison, A.G., Lin, T., and Wang, P. (2020). Mechanisms of SARS-CoV-2 Transmission and Pathogenesis. Trends Immunol. *41*, 1100–1115.

Hassan, A.O., Case, J.B., Winkler, E.S., Thackray, L.B., Kafai, N.M., Bailey, A.L., McCune, B.T., Fox, J.M., Chen, R.E., Alsoussi, W.B., et al. (2020). A SARS-CoV-2 Infection Model in Mice Demonstrates Protection by Neutralizing Antibodies. Cell *182*, 744–753.e4.

Heaney, C.D., Pisanic, N., Randad, P.R., Kruczynski, K., Howard, T., Zhu, X., Littlefield, K., Patel, E., Shrestha, R., Laeyendecker, O., et al. (2021). Comparative performance of multiplex salivary and commercially available serologic assays to detect SARS-CoV-2 IgG and neutralization titers. medRxiv. https://doi.org/10.1101/2021.01.28.21250717.

Hu, J., Gao, Q., He, C., Huang, A., Tang, N., and Wang, K. (2020). Development of cell-based pseudovirus entry assay to identify potential viral entry inhibitors and neutralizing antibodies against SARS-CoV-2. Genes Dis. *7*, 551–557.

Jangra, S., Ye, C., Rathnasinghe, R., Stadlbauer, D., Krammer, F., Simon, V., Martinez-Sobrido, L., Garcia-Sastre, A., and Schotsaert, M. (2021). The E484K mutation in the SARS-CoV-2 spike protein reduces but does not abolish neutralizing activity of human convalescent and post-vaccination sera. medRxiv. https://doi.org/10.1101/2021.01.26.21250543.

Jia, W., Wang, J., Sun, B., Zhou, J., Shi, Y., and Zhou, Z. (2021). The Mechanisms and Animal Models of SARS-CoV-2 Infection. Front. Cell Dev. Biol. *9*, 578825.

Katz, L.M. (2021). (A Little) Clarity on Convalescent Plasma for Covid-19. N. Engl. J. Med. *384*, 666–668.

Klein, S.L., Pekosz, A., Park, H.S., Ursin, R.L., Shapiro, J.R., Benner, S.E., Littlefield, K., Kumar, S., Naik, H.M., Betenbaugh, M.J., et al. (2020). Sex, age, and hospitalization drive antibody responses in a COVID-19 convalescent plasma donor population. J. Clin. Invest. *130*, 6141–6150.

Korber, B., Fischer, W.M., Gnanakaran, S., Yoon, H., Theiler, J., Abfalterer, W., Hengartner, N., Giorgi, E.E., Bhattacharya, T., Foley, B., et al.; Sheffield COVID-19 Genomics Group (2020). Tracking Changes in SARS-CoV-2 Spike: Evidence that D614G Increases Infectivity of the COVID-19 Virus. Cell *182*, 812–827.e19.

Li, Q., Wu, J., Nie, J., Zhang, L., Hao, H., Liu, S., Zhao, C., Zhang, Q., Liu, H., Nie, L., et al. (2020). The Impact of Mutations in SARS-CoV-2 Spike on Viral Infectivity and Antigenicity. Cell *182*, 1284–1294.e9.

Mahase, E. (2021). Covid-19: Novavax vaccine efficacy is 86% against UK variant and 60% against South African variant. BMJ *372*, n296.

McCray, P.B., Jr., Pewe, L., Wohlford-Lenane, C., Hickey, M., Manzel, L., Shi, L., Netland, J., Jia, H.P., Halabi, C., Sigmund, C.D., et al. (2007). Lethal infection of K18-hACE2 mice infected with severe acute respiratory syndrome coronavirus. J. Virol. *81*, 813–821.

Muik, A., Wallisch, A.K., Sänger, B., Swanson, K.A., Mühl, J., Chen, W., Cai, H., Maurus, D., Sarkar, R., Türeci, Ö., et al. (2021). Neutralization of SARS-CoV-2 lineage B.1.1.7 pseudovirus by BNT162b2 vaccine-elicited human sera. Science *371*, 1152–1153.

Muñoz-Fontela, C., Dowling, W.E., Funnell, S.G.P., Gsell, P.S., Riveros-Balta, A.X., Albrecht, R.A., Andersen, H., Baric, R.S., Carroll, M.W., Cavaleri, M., et al. (2020). Animal models for COVID-19. Nature *586*, 509–515.

Patel, E.U., Bloch, E.M., Clarke, W., Hsieh, Y.H., Boon, D., Eby, Y., Fernandez, R.E., Baker, O.R., Keruly, M., Kirby, C.S., et al. (2021). Comparative Performance of Five Commercially Available Serologic Assays To Detect Antibodies to SARS-CoV-2 and Identify Individuals with High Neutralizing Titers. J. Clin. Microbiol. *59*, e02257-20.

Plante, J.A., Liu, Y., Liu, J., Xia, H., Johnson, B.A., Lokugamage, K.G., Zhang, X., Muruato, A.E., Zou, J., Fontes-Garfias, C.R., et al. (2021). Spike mutation D614G alters SARS-CoV-2 fitness. Nature *592*, 116–121.

Roy Wong, L.Y., Zheng, J., Wilhelmsen, K., Li, K., Ortiz, M.E., Schnicker, N.J., Pezzulo, A.A., Szachowicz, P.J., Klumpp, K., Aswad, F., et al. (2021). Eicosanoid signaling as a therapeutic target in middle-aged mice with severe COVID-19. bioRxiv. https://doi.org/10.1101/2021.04.20.440676.

Sabino, E.C., Buss, L.F., Carvalho, M.P.S., Prete, C.A., Jr., Crispim, M.A.E., Fraiji, N.A., Pereira, R.H.M., Parag, K.V., da Silva Peixoto, P., Kraemer, M.U.G., et al. (2021). Resurgence of COVID-19 in Manaus, Brazil, despite high seroprevalence. Lancet *397*, 452–455.

Santos, J.C., and Passos, G.A. (2021). The high infectivity of SARS-CoV-2 B.1.1.7 is associated with increased interaction force between Spike-ACE2 caused by the viral N501Y mutation. bioRvix. https://doi.org/10.1101/2020.12.29.424708.

Shang, J., Wan, Y., Luo, C., Ye, G., Geng, Q., Auerbach, A., and Li, F. (2020a). Cell entry mechanisms of SARS-CoV-2. Proc. Natl. Acad. Sci. USA *117*, 11727–11734.

Shang, J., Ye, G., Shi, K., Wan, Y., Luo, C., Aihara, H., Geng, Q., Auerbach, A., and Li, F. (2020b). Structural basis of receptor recognition by SARS-CoV-2. Nature *581*, 221–224.

Singh, A., Singh, R.S., Sarma, P., Batra, G., Joshi, R., Kaur, H., Sharma, A.R., Prakash, A., and Medhi, B. (2020). A Comprehensive Review of Animal Models for Coronaviruses: SARS-CoV-2, SARS-CoV, and MERS-CoV. Virol. Sin. *35*, 290–304.

Sterlin, D., Mathian, A., Miyara, M., Mohr, A., Anna, F., Claër, L., Quentric, P., Fadlallah, J., Devilliers, H., Ghillani, P., et al. (2021). IgA dominates the early neutralizing antibody response to SARS-CoV-2. Sci. Transl. Med. *13*, eabd2223.

Sun, J., Zhuang, Z., Zheng, J., Li, K., Wong, R.L., Liu, D., Huang, J., He, J., Zhu, A., Zhao, J., et al. (2020). Generation of a Broadly Useful Model for COVID-19 Pathogenesis, Vaccination, and Treatment. Cell *182*, 734–743.e5.

Wang, P., Nair, M.S., Liu, L., Iketani, S., Luo, Y., Guo, Y., Wang, M., Yu, J., Zhang, B., Kwong, P.D., et al. (2021a). Antibody resistance of SARS-CoV-2 variants B.1.351 and B.1.1.7. Nature *593*, 130–135.

Wang, Z., Schmidt, F., Weisblum, Y., Muecksch, F., Barnes, C.O., Finkin, S., Schaefer-Babajew, D., Cipolla, M., Gaebler, C., Lieberman, J.A., et al. (2021b). mRNA vaccine-elicited antibodies to SARS-CoV-2 and circulating variants. Nature *592*, 616–622.

Wang, Z., Schmidt, F., Weisblum, Y., Muecksch, F., Barnes, C.O., Finkin, S., Schaefer-Babajew, D., Cipolla, M., Gaebler, C., Lieberman, J.A., et al. (2021c). mRNA vaccine-elicited antibodies to SARS-CoV-2 and circulating variants. bioRxiv. https://doi.org/10.1101/2021.01.15.426911.

Whitt, M.A. (2010). Generation of VSV pseudotypes using recombinant ΔG-VSV for studies on virus entry, identification of entry inhibitors, and immune responses to vaccines. J. Virol. Methods *169*, 365–374.

WHO (2021a). Covid-19 Response FundDonateWHO Coronavirus (COVID-19) Dashboard, https://covid19.who.int/.

WHO (2021b). COVID-19 vaccine tracker and landscape, https://www.who.int/publications/m/item/draft-landscape-of-covid-19-candidate-vaccines.

WHO (2021c). Tracking SARS-CoV-2 variants, https://www.who.int/en/activities/tracking-SARS-CoV-2-variants/.

Yan, R., Zhang, Y., Li, Y., Xia, L., Guo, Y., and Zhou, Q. (2020). Structural basis for the recognition of SARS-CoV-2 by full-length human ACE2. Science *367*, 1444–1448.

Yurkovetskiy, L., Wang, X., Pascal, K.E., Tomkins-Tinch, C., Nyalile, T., Wang, Y., Baum, A., Diehl, W.E., Dauphin, A., Carbone, C., et al. (2020). SARS-CoV-2 Spike protein variant D614G increases infectivity and retains sensitivity to antibodies that target the receptor binding domain. Cell *183*, 739–751.

Zhang, W., Davis, B.D., Chen, S.S., Sincuir Martinez, J.M., Plummer, J.T., and Vail, E. (2021). Emergence of a Novel SARS-CoV-2 Variant in Southern California. JAMA *325*, 1324–1326.

Zost, S.J., Gilchuk, P., Case, J.B., Binshtein, E., Chen, R.E., Nkolola, J.P., Schäfer, A., Reidy, J.X., Trivette, A., Nargi, R.S., et al. (2020). Potently neutralizing and protective human antibodies against SARS-CoV-2. Nature *584*, 443–449.

STAR★METHODS

KEY RESOURCES TABLE

REAGENT or RESOURCE	SOURCE	IDENTIFIER
Antibodies		
Anti-human IgG-PE secondary antibody	Invitrogen	Catalog # **62-8420;** RRID: AB_2533962
HRP-conjugated anti-human IgG, IgM, IgA (H+L)	Invitrogen	Catalog # A18847; RRID: AB_2535624
Anti-INFAR-1 (MAR1-5A3)	Bio X Cell	Catalog # BE0241; RRID: AB_2687723
Anti-RBD primary antibody	Sino Biological	Catalog # 40592-T62
HRP-conjugated goat anti-rabbit IgG secondary antibody	Invitrogen	Catalog # 31402 RRID: AB_228395
Anti-His secondary antibody	BioLegend	Catalog # 652502; RRID: AB_2556553
Anti-VSV-G	ATCC	Catalog # CRL-2700
Bacterial and virus strains		
rVSV-dG/G* luciferase	Kerafast	Catalog # EH1020-PM
rVSV-dG/G* GFP	Kerafast	Catalog # EH1019-PM
Recombinant adenoviral vectors expressing human ACE2 (AdV-hACE2)	University of Iowa Viral Vector Core	Ad5CMVhACE2; VVC-McCray-7723
WT (no 19del), WT, D614G, N501Y (no 19del), N501Y, N501Y + D614G, N501Y + L452R + D614G, or N501Y + K417N +E484K + D614G, N501Y + D614G + K417N + L452R +E484K, N501Y + D614G + K417N + L452R + E484Q PsVs	This Paper	N/A
Biological samples		
COVID 19+ human plasma	Stem Cells	Lot# 2008421004; 2009418006; 2006417008; 2009418001
COVID 19+ human plasma	RayBiotech	PS362; PS364
COVID 19+ human plasma	This Paper	N/A
Vaccinated human plasma	This Paper	N/A
Control human plasma	Pennsylvania Plasma	N/A
Chemicals, peptides, and recombinant proteins		
RBD-Fc	This paper	N/A
RBD-His	This paper	N/A
N501Y-RBD-His	Sino Biological	Catalog# 40592-V08H82
N501Y-RBD-Fc	This paper	N/A
MPL	Sigma Aldrich	SAB1406140
D-luciferin	GoldBio	Catalog # eLUCNA-100; CAS # 103404-75-7
Hoechst 33342	Invitrogen	Catalog # H3570
Prolong Glass	Invitrogen	Catalog # P36980
Zombie Aqua Viability Dye	BioLegend	Catalog # 423101
Human TruStain FcX	BioLegend	Catalog # 422301
Critical commercial assays		
Expi293F expression system kit	Thermo Fisher Scientific	Catalog # A14635
4-15% Tris-glycine SDS-PAGE gels	Bio-Rad	Catalog # 4568033
Pierce BCA Protein Assay Kit	Thermo Fisher Scientific	Catalog # A53225
Luciferase assay kit	Promega	Catalog # E1500
Lipofectamine 3000	Thermo Fisher Scientific	Catalog # L3000001

(*Continued on next page*)

Continued

REAGENT or RESOURCE	SOURCE	IDENTIFIER
Deposited data		
RBD in complex with mouse ACE2	Brooke and Prischi, 2020	https://github.com/fprischi/Supplementary_ComplexesStructures
Experimental models: Cell lines		
293 TT cells	ATCC	CRL-3467
BHK-21 cells	ATCC	CCL-10
Experimental models: Organisms/strains		
BALB/c	Charles River	Strain code: 028 BALB/cAnNCrl
C57BL/6	Taconic	Model: B6-F C57BL/6NTac
Oligonucleotides		
Primers for generating SARS-CoV2 spike sequence or mutant PsV plasmid, see Table S1	Integrated DNA Technologies	N/A
Recombinant DNA		
pCMV3-SARS-CoV-2-S	Sino Biological Inc. Beijing, China	Catalog # VG40592-UT
pFuse-mIgG2a-Fc2	Invivogen	pfuse-mg2afc2
pCMV3-SARS-CoV-2-S-N501Y	This paper	N/A
pCMV3-SARS-CoV-2-S-cd19	This paper	N/A
pCMV3-SARS-CoV-2-S-N501Y-cd19	This paper	N/A
pCMV3-SARS-CoV-2-S-cd19-D614G	This paper	N/A
pCMV3-SARS-CoV-2-S-cd19-D614G-N501Y	This paper	N/A
pCMV3-SARS-CoV-2-S-cd19-D614G-N501Y-K417N-E484K	This paper	N/A
pCMV3-SARS-CoV-2-S-cd19-D614G-N501Y-K417N-L452R-E484Q	This paper	N/A
pCMV3-SARS-CoV-2-S-cd19-D614G-N501Y-L452R	This paper	N/A
pfuse-RBD-mIgG2aFc	This paper	N/A
pfuse-RBD-N501Y-mIgG2aFc	This paper	N/A
Software and algorithms		
CytExpert	Beckman Coulter	https://www.beckman.com/flow-cytometry/instruments/cytoflex/software
Gen5	Biotek Instruments	https://www.biotek.com/products/software-robotics-software/gen5-microplate-reader-and-imager-software/
Living Image	Xenogen	https://www.perkinelmer.com/product/spectrum-200-living-image-v4series-1-128113
NIS-Elements	Nikon	https://www.microscope.healthcare.nikon.com/products/software/nis-elements
Image Lab	BioRad	https://www.bio-rad.com/en-us/product/image-lab-software?ID=KRE6P5E8Z
PyMOL	Schrödinger, Inc.	https://pymol.org/2/
Prism	GraphPad	https://www.graphpad.com/scientific-software/prism/
GloMax-Multi+ Detection System with Instinct	Promega	https://www.promega.com/resources/protocols/technical-manuals/101/glomax-multi-detection-system-with-instinct-software-protocol/

RESOURCE AVAILABILITY

Lead contact

Further requests for information for reagents should be directed to Dr. Chien-Fu Hung (chung2@jhmi.edu), our lead contact, and they will be fulfilled within reasonable request.

Materials availability

Plasmids generated that were used for PsV production are available upon request. Their production method has been provided in the manuscript. There are no other new materials generated in this manuscript.

Data and code availability

- All data reported in this paper will be shared by the lead contact upon request.
- This paper does not report original code.
- Any additional information required to reanalyze the data reported in this paper is available from the lead contact upon request.

EXPERIMENTAL MODEL AND SUBJECT DETAILS

Animals

6-8-week-old female BALB/c and C57BL/6 mice were purchased from Charles River Laboratories (Frederick, Maryland, USA) and Taconic (Cambridge City, IN), respectively. All mice were maintained at the Johns Hopkins University School of Medicine Oncology Animal Facility in Cancer Research Building II (Baltimore, MD) under specific-pathogen-free conditions. The housing and handling of mice follow guidelines established by Johns Hopkins Medical Institutions Animal Care and Use Committee and the National Institutes of Health. All animals were performed according to approved protocols by the Johns Hopkins Institutional Animal Care and Use Committee and in accordance with recommendations for proper use and care of laboratory animals. Animals are monitored daily for infection and other illnesses by trained animal technicians. Only trained laboratory personnel and animal technicians were allowed to handle laboratory animals. All individuals handling mice were registered to protocols at the Johns Hopkins Animal Care and Use Committee.

Human samples

COVID-19+ patient samples and vaccinated human samples were collected and used in accordance with approved institutional review board protocols at Johns Hopkins University. COVID-19+ participants were randomly drawn from a cohort of patients as previously described (Heaney et al., 2021; Klein et al., 2020; Patel et al., 2021). Vaccinated participants included 14 females (age 27-59) and 1 male (age 56).

Cell lines

BHK-21 cells and 293TT cells (Buck et al., 2004) were both purchased from ATCC and maintained in low passage numbers according to ATCC guidelines at 37°C in DMEM/10% FBS. All cell lines were maintained in master cell banks and undergo routine mycoplasma testing. Any cells displaying abnormal morphological changes or doubling time are discarded and replaced with a new vial.

METHOD DETAILS

Plasmids for PsV prep

To generate the N501Y mutation PsV plasmid (pCMV3-SARS-CoV-2-S-N501Y), site-directed mutagenesis was used for generating the N501Y mutation in the SARS-CoV-2 spike sequence. PCR fragment was amplified by primers (TAATACGACTCACTATAGGG, TGGTTGGTAGCCCACTCCATAGGTTGGTTGGAAGCCATAGG, CCTATGGCTTCCAACCAACCTATGGAGTGGGCTACCAACCA, and AAATCTAGATTAACAACAGGAGCCACAGGAA) and template (pCMV3-SARS-CoV-2-S, Sino Biological Inc. Beijing, China) and cloned into PCMV3 vector.

To generate the 19del pseudovirus (PsV) plasmid (pCMV3-SARS-CoV-2-S-cd19), 19 amino acids were deleted in the spike protein sequence of SARS-CoV-2 variant Wuhan-Hu-1. PCR fragment was amplified by primers TTTGGTACCATGTTTGTGTTCCTGGTGC and AAATCTAGATTAACAACAGGAGCCACAGGAA and template (pCMV3-SARS-CoV-2-S, Sino Biological Inc. Beijing, China) and cloned into PCMV3 vector.

To generate 19del + N501Y mutation PsV plasmid (pCMV3-SARS-CoV-2-S-N501Y-cd19), site-directed mutagenesis was used for generating N501Y mutation in the SARS-CoV-2 spike sequence. PCR fragment was amplified by primers (TAATACGACTCACTA TAGGG, TGGTTGGTAGCCCACTCCATAGGTTGGTTGGAAGCCATAGG, CCTATGGCTTCCAACCAACCTATGGAGTGGGCTACCA ACCA, and AAATCTAGATTAACAACAGGAGCCACAGGAA) and template (pCMV3-SARS-CoV-2-S-cd19) and cloned into PCMV3 vector.

To generate 19del + D614G mutation PsV plasmid (pCMV3-SARS-CoV-2-S-cd19-D614G), site-directed mutagenesis was used for generating D614G mutation in the SARS-CoV-2 spike sequence. PCR fragment was amplified by primers (TAATACGACTCA CTATAGGG, GGCACCTCAGTACAGTTCACACCCTGGTAGAGCACAGCCACC, GGTGGCTGTGCTCTACCAGGGTGTGAACTGTAC TGAGGTGCC, and AAATCTAGATTAACAACAGGAGCCACAGGAA) and template (pCMV3-SARS-CoV-2-S-cd19) and cloned into PCMV3 vector.

To generate 19del + N501Y + D614G mutation PsV plasmid (pCMV3-SARS-CoV-2-S-cd19-D614G-N501Y), site-directed mutagenesis was used for generating D614G mutation in the SARS-CoV-2 spike sequence. PCR fragment was amplified by primers (TAAT ACGACTCACTATAGGG, GGCACCTCAGTACAGTTCACACCCTGGTAGAGCACAGCCACC, GGTGGCTGTGCTCTACCAGGGTGT GAACTGTACTGAGGTGCC, and AAATCTAGATTAACAACAGGAGCCACAGGAA) and template (pCMV3-SARS-CoV-2-S-N501Y-cd19) and cloned into PCMV3 vector.

To generate 19del + N501Y + D614G + L452R mutation PsV plasmid (pCMV3-SARS-CoV-2-S-cd19-D614G-N501Y-L452R), site-directed mutagenesis was used for generating L452R mutation in the SARS-CoV-2 spike sequence. PCR fragment was amplified by primers (TAATACGACTCACTATAGGG, TGGGAGGCAACTACAACTACCGCTACAGACTGTTCAGGAAGAGC, GCTCTTCCTGAACA GTCTGTAGCGGTAGTTGTAGTTGCCTCCCA, and AAATCTAGATTAACAACAGGAGCCACAGGAA) and template (pCMV3-SARS-CoV-2-S-cd19-D614G-N501Y) and cloned into PCMV3 vector.

To generate 19del + N501Y + D614G + K417N mutation PsV plasmid (pCMV3-SARS-CoV-2-S-cd19-D614G-N501Y-K417N), site-directed mutagenesis was used for generating K417N mutation in the SARS-CoV-2 spike sequence. PCR fragment was amplified by primers (TAATACGACTCACTATAGGG, TTTGTAGTTGTAGTCAGCAATGTTGCCTGTTTGTCCAGGGGC, GCCCCTGGACAAACAG GCAACATTGCTGACTACAACTACAAA, and AAATCTAGATTAACAACAGGAGCCACAGGAA) and template (pCMV3-SARS-CoV-2-S-cd19-D614G-N501Y) and cloned into PCMV3 vector.

To generate 19del + N501Y + D614G + K417N + E484K mutation PsV plasmid (pCMV3-SARS-CoV-2-S-cd19-D614G-N501Y-K417N-E484K), site-directed mutagenesis was used for generating E484K mutation in the SARS-CoV-2 spike sequence. PCR fragment was amplified by primers (TAATACGACTCACTATAGGG, GAAAGTAACAGTTGAAGCCCTTCACTCCATTACATGGTGTGC, GCACACCATGTAATGGAGTGAAGGGCTTCAACTGTTACTTTC, and AAATCTAGATTAACAACAGGAGCCACAGGAA) and template (pCMV3-SARS-CoV-2-S-cd19-D614G-N501Y-K417N) and cloned into PCMV3 vector.

To generate 19del + N501Y + D614G + K417N + L452R +E484K mutation PsV plasmid (pCMV3-SARS-CoV-2-S-cd19-D614G-N501Y-K417N-L452R-E484K), site-directed mutagenesis was used for generating L452R mutation in the SARS-CoV-2 spike sequence. PCR fragment was amplified by primers (TAATACGACTCACTATAGGG, TGGGAGGCAACTACAACTACCGCTACAG ACTGTTCAGGAAGAGC, GCTCTTCCTGAACAGTCTGTAGCGGTAGTTGTAGTTGCCTCCCA, and AAATCTAGATTAACAACAGGA GCCACAGGAA) and template (pCMV3-SARS-CoV-2-S-cd19-D614G-N501Y-K417N-E484K) and cloned into PCMV3 vector.

To generate 19del + N501Y + D614G + K417N + L452R +E484Q mutation PsV plasmid (pCMV3-SARS-CoV-2-S-cd19-D614G-N501Y- K417N-L452R-E484Q), site-directed mutagenesis was used for generating E484Q mutation in the SARS-CoV-2 spike sequence. PCR fragment was amplified by primers (TAATACGACTCACTATAGGG, GAAAGTAACAGTTGAAGCCCTGCACTCCAT-TACATGGTGTGC, GCACACCATGTAATGGAGTGCAGGGCTTCAACTGTTACTTTC, and AAATCTAGATTAACAACAGGAGCCACA GGAA) and template (pCMV3-SARS-CoV-2-S-cd19-D614G-N501Y-K417N-L452R-E484K) and cloned into PCMV3 vector.

To generate pfuse-RBD-mIgG2aFc (RBD-Fc), PCR fragment was amplified by primers (AAAGAATTCGATGAGGGTCCAACCAA CAGAG and TTTAGATCTGAAGTTCACACACTTGTTCTT) and template (pCMV3-SARS-CoV-2-S, Sino Biological Inc. Beijing, China) and cloned into pFuse-mIgG2a-Fc2 vector (Invivogen, San Diego, USA).

To generate pfuse-RBD-N501Y-mIgG2aFc, PCR fragment was amplified by primers (AAAGAATTCGATGAGGGTCCAACCAACA GAG and TTTAGATCTGAAGTTCACACACTTGTTCTT) and template (pCMV3-SARS-CoV-2-S-N501Y) and cloned into pFuse-mIgG2a-Fc2 vector (Invivogen, San Diego, USA).

Generation of HIV-I SARS-CoV-2 spike PsVs

We constructed a SARS-CoV-2 spike PsV using a lentivirus packaging system. 293TT cells were co-transfected with a packaging plasmid expressing Gag and Pol (CMVΔ8.91), a lentivirus vector expressing luciferase (pCDH1puro-LucGFP), and an expression plasmid with either pCMV3-SARS-CoV-2-S, pCMV3-SARS-CoV-2-S-N501Y, pCMV3-SARS-CoV-2-S-cd19, pCMV3-SARS-CoV-2-S-N501Y-cd19, pCMV3-SARS-CoV-2-S-cd19-D614G, or pCMV3-SARS-CoV-2-S-cd19-D614G-N501Y. All plasmids were at 1.0μg/ml and used in the following ratios: pCDH1puro-Luc, 9 μl; pCMVΔ8.91, 12 μl; and pCMV3-SARS-CoV-2-S, pCMV3-SARS-CoV-2-S-N501Y, pCMV3-SARS-CoV-2-S-cd19, pCMV3-SARS-CoV-2-S-N501Y-cd19, pCMV3-SARS-CoV-2-S-cd19-D614G, or pCMV3-SARS-CoV-2-S-cd19-D614G-N501Y, 3 μl. After 3 days of incubation at 37°C in Opti-M medium, cells were harvested and pelleted at 2000 g x 5 min. The supernatant was filtered through a 0.45 μm filter, with/or without concentration using an Amicon Ultra-15 filter unit, aliquoted, and stored at −80°C. The amount of PsV was quantified normalized across preps by SARS-CoV-2 S-protein western blot (Sino Biological Inc. Beijing, China).

Generation of VsV SARS-CoV-2 spike PsVs

BHK-21 cells (ATCC) were transfected with pCMV3-SARS-CoV-2-S, pCMV3-SARS-CoV-2-S-N501Y, pCMV3-SARS-CoV-2-S-cd19, pCMV3-SARS-CoV-2-S-N501Y-cd19, pCMV3-SARS-CoV-2-S-cd19-D614G, pCMV3-SARS-CoV-2-S-cd19-D614G-N501Y, pCMV3-SARS-CoV-2-S-cd19-D614G-N501Y-K417N-E484K, pCMV3-SARS-CoV-2-S-cd19-D614G-N501Y-K417N-L452R-E484Q,

or pCMV3-SARS-CoV-2-S-cd19-D614G-N501Y-L452R using Lipofectamine 2000 (Invitrogen). Twenty-four hours later, the transfected cells were infected with rVSV-dG/G* luciferase or rVSV-dG/G* GFP (Whitt, 2010) with a multiplicity of four. Two hours after infection, cells were washed with PBS three times, and then new Opti-M culture medium with 10% hybridoma (anti-VSV-G) supernatant (ATCC; CRL-2700) was added. Twenty-four hours post infection, the supernatant was filtered through a 0.45 μm filter, with/or without concentration using an Amicon Ultra-15 filter unit, aliquoted, and stored at −80°C.

Protein production and purification

RBD-Fc and N501Y-RBD-Fc protein was expressed using Expi293F expression system kit (Thermo Fisher Scientific, Waltham, MA) according to the manufacturer's instructions. Expi293F cells were transfected with pfuse-RBD-mIgG2aFc or pfuse-RBD-N501Y-mIgG2aFc. RBD-Fc and RBD-N501Y-Fc proteins were purified by a HiTrap protein G column (GE Healthcare Life Sciences, Marlborough, MA.

Antibody quantification by flow cytometry

In order to determine antibody levels, 1e5 hACE2+ 293 cells were incubated with human plasma samples for 30 minutes at 4 degrees. Cells were washed in FACS buffer, and then stained with an anti-human IgG-PE secondary antibody for 30 minutes at 4 degrees. Were then again washed extensively in FACS buffer, fixed with 4% PFA/PBS for 10 minutes, then acquired on a Beckman Coulter CytoFLEX S. Background signal was normalized to secondary alone and normal human plasma controls. MFI values were then determined using CytExpert software (Beckman Coulter).

Antibody characterization by ELISA

To determine anti-WT or N501Y + K417N + E484K + D614G RBD IgG, IgM, and IgA antibody levels, ELISA plates were coated with either WT or N501Y + K417N + E484K + D614G RBD protein at a concentration of 2 ug/ml overnight in PBS. Plates were washed with 0.05% Tween-20 in PBS, blocked with 10% FBS in PBS, and then incubated for 2 hours with human plasma samples titrated with 10% FBS in PBS. After washing, wells were incubated with biotin conjugated + HRP or HRP-conjugated anti-human IgG, IgM, or IgA (Invitrogen). After washing, plates were incubated with ultra TMB substrate (Thermo Fisher). Reaction was stopped with 2M H2SO4 and absorbance was read at 450nm and 590nm as a reference.

Mouse experiments

Recombinant adenoviral vectors expressing human ACE2 (AdV-hACE2) were purchased from the University of Iowa Viral Vector Core. For PsV infection, mice were first treated with $2.5x10^8$ PFU of AdV-hACE2 via i.n. administration where appropriate. Three days after AdV transduction, mice were treated with 500ug of anti-INFAR-1 (MAR1-5A3). 24-hours later, normalized amounts of WT (no 19del), WT, D614G, N501Y (no 19del), N501Y, N501Y + D614G, N501Y + L452R + D614G, or N501Y + K417N +E484K + D614G PsVs were treated intranasally in a volume of 50ul, followed by 30uL of PBS wash intranasally. For blocking experiments, normal or COVID 19+ human plasma was purchased from Stem Cells and RayBiotech. RBD-Fc mouse plasma was taken from RBD-Fc vaccinated mice which were treated intranasally with 2 doses of 30ug RBD-Fc and 5ug of MPL 2-weeks apart. 30uL of plasma was treated i.n. an hour prior to PsV infection. *In vivo* bioluminescence imaging was performed using the IVIS Series 2000 (PerkinElmer) to determine infection in the nasopharynx and lungs. The mice were treated with 100 ug of D-luciferin (GoldBio) through retro-orbital injections followed by 80 ug delivered intranasally. 5 minutes after D-luciferin administration, mice were imaged on the IVIS Spectrum with the following settings: 5-minute exposure, excitation filter blocked, emission filter open, FOV 22.7, Binning: 8. Luminescent signals from the nasopharynx and lungs are quantified as average radiance using Living Image 3.0 Software (Xenogen). Data are represented on linear scales. This allows results obtained to be easier to visualize on a graph because the dynamic range of data generated on the IVIS is somewhat limited. Mice were imaged starting at 24-hours post infection.

Microscopy

For confirmation of infection in the airway, lungs were collected 24-hours post infection with either D614G or N501Y + D614G GFP+ VsV PsVs. Samples were fixed in 4% PFA for 6 hours followed by cryoprotection in 10% sucrose for 2 hours, 2s0% sucrose for 2 hours, and then 30% sucrose overnight. Next, samples were washed and frozen in OCT. Tissue was then sectioned at 8 micron by the oncology tissue services core at Johns Hopkins. Slides were then rehydrated in PBS for 15 minutes, stained with Hoechst 33342, mounted in Prolong Glass (Invitrogen), and imaged on a te-2000 microscope with deconvolution (Nikon).

RBD and ACE2 structure visualization

The 3D structures of RBD in complex with human ACE2 were retrieved from the RCSB Protein Data Bank (PDB: 6M17) (Yan et al., 2020). The 3D structures of RBD in complex with mouse ACE2 homology model were retrieved from https://github.com/fprischi/Supplementary_ComplexesStructures (Brooke and Prischi, 2020). All structures were visualized using PyMOL.

RBD and RBD-Fc protein quality assessment

Purity of RBD-Fc and RBD-His variant proteins was determined by SDS-PAGE. Briefly, protein concentration was measured by Pierce BCA Protein Assay Kit (Thermo Scientific). One ug protein was treated with 4X Laemlli Sample Buffer (BioRad) containing

β-mercaptoethanol and boiled at 100°C for 5 minutes. Proteins were separated on 4%–15% Tris-glycine SDS-PAGE gels, stained with Coomassie blue at room temperature for 1 hour, and de-stained with water at room temperature overnight. Images were collected on a chemidoc (BioRad)

PsV quantification

RBD expression in lentivirus and VsV PsVs was measured and normalized by western blot. Briefly, 21 uL PsVs were treated with 4X Laemlli Sample Buffer (BioRad) containing β-mercaptoethanol and boiled at 100°C for 10 minutes. Proteins were separated on 4%–15% Tris-glycine SDS-PAGE gels and transferred to nitrocellulose membranes. Blots were blocked with blocking buffer (5% BSA and 0.05% Tween 20 in TBS) at room temperature for 30 minutes and incubated with anti-RBD primary antibody (1:2000, Sino Biological) at 4°C overnight. Blots were then incubated with HRP-conjugated goat anti-rabbit IgG secondary antibody (1:10000) at room temperature for 1 hour and visualized with Pico Plus Chemiluminescent Substrate (Thermo Scientific).

Binding affinity assay

293 cells stably transfected with human or mouse ACE2 were stained with Zombie Aqua Viability Dye (1:100, BioLegend) and Human TruStain FcX (1:50, BioLegend) at 4°C for 15 minutes and transferred to 96-well plates (10^5 cells per well). Cells were then incubated with WT or N501Y-RBD-His (Sino Biological) at various dilutions at 4°C for 30 minutes and stained with anti-His secondary antibody (1:50, BioLegend) at 4°C for 15 minutes. Cells were then fixed with 4% PFA at room temperature for 5 minutes and analyzed by flow cytometry. K_D values of RBD binding affinities for ACE2 were calculated using binding curves fitted in GraphPad.

In vitro infection assay

293 cells stably transfected with human ACE2, mouse ACE2, or neither were seeded in 96-well plates (10^4 cells per well) and incubated at 37°C for 24 hours. Cells were then incubated with lentivirus or VsV PsVs expressing RBD-luciferase variants at various dilutions at 37°C for 48 hours. Cell lysates were generated by adding 5X Reporter Lysis Buffer (Promega) and shaking at 600 rpm at room temperature for 30 minutes. Luciferase activity in cell lysates was determined with a luciferase assay kit (Promega) according to the manufacturer's instructions. Bioluminescence was measured using a GloMax Multi Detection System (Promega).

In vitro blocking assay

293 cells stably transfected with human ACE2, mouse ACE2, or neither were seeded in 96-well plates (10^4 cells per well) and incubated at 37°C for 24 hours. Plasma was collected from COVID-19+ or vaccinated human donors and control (StemCell or Ray Biotech) or RBD-Fc vaccinated mice. Equal amounts of Lentivirus or VsV PsVs expressing RBD-luciferase variants were mixed with plasma at various dilutions at room temperature for 1 hour. Cells were then infected with pre-incubated PsVs at 37°C for 48 hours. Cell lysates were generated by adding 5X Reporter Lysis Buffer (Promega) and shaking at 600 rpm at room temperature for 30 minutes. Luciferase activity in cell lysates was determined with a luciferase assay kit (Promega) according to the manufacturer's instructions. Bioluminescence was measured using a GloMax Multi Detection System (Promega). Percent neutralization was calculated based on the luminescence of cells infected with PsVs and plasma from normal human donors. Reciprocal IC_{50} titers were determined using a four-parameter logistic curve in GraphPad.

QUANTIFICATION AND STATISTICAL ANALYSIS

All data are expressed as means ± standard error of the mean (SEM). Results between PsV infection groups or blocking conditions were evaluated by analysis of variance (one-way ANOVA). All P values < 0.05 were considered significant. Of note, *, **, and *** indicate P values less than 0.05, 0.01, and 0.001, respectively; N.S., not significant. Specific n = experiments are indicated in the figure legends in quantity and meaning. Experiments were repeated at least once, for a total of 2 independent experiments. A representative experiment comprising of the indicated number of n is shown. All statistical calculations were performed in GraphPad Prism 9.